Thermodynamic Dissection of the Ezrin FERM/CERMAD Interface†

Bhargavi Jayaraman and Linda K. Nicholson*

Department of Molecular Biology and Genetics, Cornell University, Ithaca, New York 14853

Received June 29, 2007; Revised Manuscript Received August 7, 2007

ABSTRACT: ERM (Ezrin−Radixin−Moesin) proteins are key cross-linkers of the plasma membrane and the actin cytoskeleton. They are regulated by the intramolecular association of the N-terminal FERM (band-four point one, Ezrin, Radixin, Moesin) and C-terminal CERMAD (ERM association domain) domains (N/C interaction), which masks the binding surfaces of the domains for other molecules. The N/C interface is characterized by the highly distributed binding of CERMAD through a β-strand and four α-helices to a globular FERM. Though it is a target for multiple regulatory signals, little is known about the dynamics/thermodynamics governing this interface. Recent implications of Ezrin in cancer metastasis have increased the necessity to understand this regulatory switch. In this study, we report residue-specific stabilities of Ezrin CERMAD at the Ezrin N/C interface obtained using hydrogen−deuterium exchange NMR. These stabilities vary across secondary structural elements and identify F583 and L586 as key anchor residues for the most stable element, αD. Macroscopic N/C binding energetics, obtained using isothermal titration calorimetry (ITC) reveals a high affinity (K_d =176 nM) enthalpy-driven binding (ΔH = −26 kcal/mol, $T\Delta S$ = −17 kcal/mol) at 25 °C at pH 7 in MES and phosphate buffers. A 10-fold increase in affinity was observed for measurements in acetate buffer, suggesting that an acetate-like molecule might promote the repressed form of the complex, possibly through interaction with the F2 subdomain of FERM, which resembles the acyl-CoA binding protein. In summary, our results have illustrated the dynamic nature of this regulatory interface and provide a foundation for investigating the role of regulatory signals on the stability of this interface.

While many different cancer types have been identified and studied, the biological and molecular mechanisms underlying their metastatic spread are very similar. With metastasis responsible for a majority of cancer deaths, significant effort has been dedicated to the identification of the molecules and the establishment of the connections between different events involved in this elaborate phenomenon (*1*). Ezrin is one such molecule that has been recently implicated in transformation, metastasis and tumor progression from microarray data (*2*−*4*), cultured cells (*4*−*6*), and mouse model systems (*3*, *6*).

Ezrin is a member of the Ezrin−Radixin−Moesin (ERM[1]) family of proteins that are directly involved in regulated interactions between the actin cytoskeleton and the plasma membrane. These interactions are required for basic cellular activities that include control of cell morphology, vectorial transport of ions and nutrients, reception and transduction of signals involved in cell−cell communication, cell motility and survival, and adhesion to adjacent cells or the extracellular matrix (*7*). Among the myriad interacting partners of Ezrin are adhesion molecules such as CD44 (*8*, *9*) and ICAM-1 and 2 (*9*, *10*), adapter molecules such as EBP50 (*11*) and E3KARP (*11*, *12*), and signaling molecules such as RhoGDI (*13*), Dbl (*14*) and FAK (*15*). It thus serves as a molecular hub, linking and controlling different cellular signaling events (*16*). Since all the above activities are also associated with the metastatic capabilities of cells, a complete understanding of Ezrin function and regulation is vital to its future role as a possible diagnostic marker and/or therapeutic metastatic target.

ERM proteins are composed of a C-terminal tail domain (CERMAD, ∼110 residues) that binds to cortical f-actin filaments, an N-terminal FERM (band Four-point-one, Ezrin-Radixin-Moesin homology, ∼300 residues) domain that binds to plasma membrane proteins (*17*), and a central α-helical domain, whose structure and possible roles in ERM protein function have only recently come to light (*18*). The FERM domain localizes the ERM proteins to the plasma membrane where they have dynamic and regulatory roles in membrane-associated processes (*7*, *16*). It either directly binds to cytoplasmic domains of transmembrane proteins such as CD44 (*9*) or indirectly through adapter proteins such as EBP50 (*19*). Through the two separate binding functions of the FERM and CERMAD domains, ERM proteins dynamically cross-link the plasma membrane to the cortical cytoskeleton, and lie at the heart of dynamic membrane functions such as endocytosis, exocytosis, and cortical signaling.

The cross-linking function of ERM proteins is regulated by an intramolecular FERM/CERMAD interaction that masks their respective intermolecular binding surfaces (*17*).

† This work was funded by National Science Foundation Grant MCB-0212597 to L.K.N.

* Corresponding author. Tel: (607) 255-7208. Fax: (607) 255-6249. E-mail: lkn2@cornell.edu.

[1] Abbreviations: ERM, ezrin radixin moesin; FERM, band-four point one, Ezrin, Radixin, Moesin; CERMAD, carboxyl terminal Ezrin−Radixin−Moesin association domain; PIP_2, phosphatidylinositol-4,5-bisphosphate; HX, hydrogen−deuterium exchange; NMR, nuclear magnetic resonance; HSQC, heteronuclear single quantum correlation; ITC, isothermal titration calorimetry.

10.1021/bi701281e CCC: $37.00
Published on Web 10/03/2007

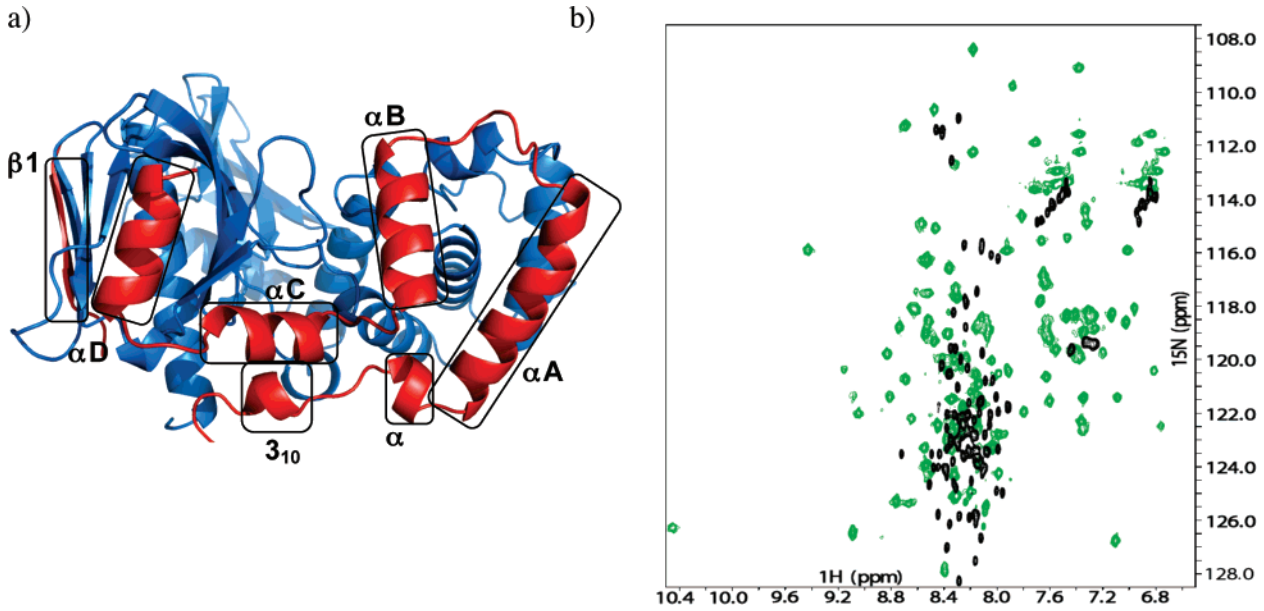

FIGURE 1: (a) Homology model of the Ezrin FERM (blue)/CERMAD (red) complex. The secondary structural elements of CERMAD are marked in the model. (b) ^{1}H-^{15}N HSQC overlay of free (MW, 13.2 kDa; black) and bound CERMAD (MW of complex, 48 kDa; green).

This intramolecular N/C association is weakened both by phosphorylation of a specific threonine in CERMAD (T558 in Moesin, T567 in Ezrin, and T564 in Radixin) (*20*−*22*) and by binding of phosphatidylinositol-4,5-bisphosphate (PIP_2) to FERM (*23*). While significant information is available on the mechanisms of activating ERM proteins, little is currently known about the cellular signals and signaling molecules that might be involved in promoting the repressed state.

The X-ray crystal structure of the noncovalent Moesin FERM/CERMAD complex (referred to hereafter as the N/C complex) revealed that FERM (297 residues) is composed of three subdomains: F1 (residues 4−82) resembles ubiquitin, F2 (residues 96−195) resembles acyl-CoA binding protein, and F3 (residues 204−297) resembles the PTB (phosphotyrosine binding), PH (plextrin homology), and EVH1 (enabled/VASP homology 1) domains (*17*). In contrast, CERMAD (residues 488−577) does not adopt a globular structure but binds in five distinct, apparently independent interactions. The CERMAD fold comprises five major elements: one β-strand (β1) and four α-helices (αA-αD). Additionally, a 20-residue segment between β1 and αA contains one turn each of a 3_{10} helix (3_{10}) and an α helix (α) (Figure 1a). These CERMAD elements are spread over a large interface and bury 2700 Å^2 of the FERM surface. On the basis of this structure, it was predicted that each of these five elements would contribute to the tight binding of CERMAD to FERM (*17*).

Numerous biochemical, cell biological, and structural studies have contributed toward the understanding of the regulatory mechanisms controlling this interface. While X-ray structures have provided high-resolution maps of ERM proteins, the pictures they portray are static and relative stabilities of the different regions of the interface can only be predicted from the observed structural interactions. Consequently, our understanding does not yet include a dynamic or thermodynamic description of this unusual binding interface. Currently, neither the measured affinity of CERMAD for FERM nor the relative stabilities of its five secondary structural elements are known. Local stability is particularly critical in extended binding interfaces such as those found in the ERM family of proteins, especially considering that each of these regions might be targets of different regulatory signals. NMR is a powerful tool for examining the thermodynamics of interactions on a residue-specific basis, while isothermal titration calorimetry (ITC) provides a macroscopic description of the thermodynamics of the system.

Here, we report both a microscopic, residue-specific evaluation of CERMAD stability in the Ezrin N/C complex obtained using hydrogen−deuterium exchange (HX) NMR experiments and the macroscopic thermodynamics of the system obtained using ITC. A hierarchy of stability is observed among the five secondary structural elements, with the C-terminal residue of CERMAD being the most stable residue, reflecting the macroscopic ΔG_{bind}. Functional relevance of the observed local stabilities are discussed in relation to the global, macroscopic binding thermodynamics of the system. These studies have also yielded a serendipitous result suggesting a mechanism by which a small molecule might promote the repressed form of the complex. Given the high level of sequence identity (*7*) and functional redundancy of ERM family members (*24*, *25*), knowledge gained from these studies of the N/C interaction in Ezrin should be of general applicability to Moesin and Radixin.

MATERIALS AND METHODS

Construction of the Ezrin FERM/CERMAD Complex Homology Model. Among the currently available structures, the structure of the N/C complex exists only for Moesin (PDB-ID 1EF1 (*17*) and 2I1J (*18*)). However, the high sequence identity between the Ezrin and Moesin sequences (67% identity for CERMAD and 87% for FERM) allowed the construction of a homology model of the Ezrin FERM/CERMAD complex. Although a crystal structure of the active Ezrin FERM is available (PDB-ID 1NI1), the structural differences between the active and dormant FERM domains, as detailed in Smith et al. (*26*), require that a model for the

dormant Ezrin FERM domain be built. The sequence alignments between Ezrin and Moesin CERMADs (aa 497−586 in Ezrin) and Ezrin and Moesin FERMs (aa 1−297 in Ezrin) and the structure of the dormant Moesin N/C complex (PDB-ID 1EF1) published in Pearson et al. (*17*) were used for the construction of the Ezrin homology model. Homology models for dormant Ezrin FERM and bound CERMAD were constructed separately using Swiss-Model (*27*, *28*). A structural model for the Ezrin N/C complex was then generated using Swiss-Pdb viewer (*29*) as follows. The resulting Ezrin FERM and CERMAD models were each structurally aligned with their corresponding domains in the dormant Moesin N/C complex (PDB-ID 1EF1) using the Magic Fit function, and the Ezrin residues were then selected and merged into a single layer using the Create merged layer from selection function. Then, the new layer was saved as a single pdb file to form the final model for the complex (Figure 1a).

Protein Expression and Purification. The CERMAD gene (residues 475−586, a gift from Professor Anthony Bretscher, Molecular Biology and Genetics, Cornell University, Ithaca, NY) was cloned into a pET28 a(+) expression vector with an amino terminal 6-His tag and a HRV 3c protease recognition sequence inserted between the tag and protein (*30*). The protein was expressed in BL21 DE3 *E. coli* cells at 37 °C in M9 minimal medium in the presence of 30 μg/mL kanamycin (Sigma) and purified from a 1.5 L culture. For isotopic labeling, cells were grown in sterile filtered M9 medium made up in 99.96% D_2O (Cambridge Isotope Laboratories, Inc.), containing 1 g/L ^{15}N NH_4Cl (Spectra Stable Isotopes) and/or 3 g/L ^{13}C D-Glucose (Cambridge Isotope Laboratories, Inc.). In order to acclimate cells to deuterated medium, the cells were first grown overnight in 5 mL of LB medium with 25% D_2O. Then 50 μL of this culture was transferred into 5 mL of M9 medium in 50% D_2O and grown for 24 h. This procedure was repeated with 75% D_2O. Finally, 2 × 0.5 mL of the 75% D_2O M9 culture was added to 2 × 50 mL of M9 medium and ∼99% D_2O, and grown for 24 h. Each 50 mL culture was added to 700 mL of ∼99% D_2O M9 media in a 2.8 L baffled flask. The cells were grown with vigorous shaking and induced with 1 mM IPTG (Acros Organics) at OD_{600nm} of 1.1. Cells were harvested 3 h after induction by centrifugation (5000*g*) at 4 °C for 10 min and were stored at −80 °C for future use. All purification steps were carried out at 4 °C. The frozen cells were thawed on ice and lysed in 30 mL of buffer A (50 mM NaH_2PO_4, 300 mM NaCl, and 5 mM Imidazole at pH 8.0), supplemented with 60 μL of protease inhibitor (PI) cocktail (Sigma), 1 mM PMSF (Sigma), and 1 mg/mL of lysozyme (Sigma). The lysed cells were sonicated and cleared by centrifugation at 11,000*g* for 40 min. The supernatant was filtered (0.8 micron filter) and passed over 3 mL bed volume of Ni beads (Qiagen) equilibrated in buffer A. The column was washed in 20 bed volumes of buffer A and 20 bed volumes of buffer B (50 mM NaH_2PO_4, 300 mM NaCl, and 10 mM imidazole at pH 8.0).

The 3c protease gene was amplified from the HRV-14 viral genome (a gift from Professor Glyn Stanway, University of Essex, U.K.) and cloned into a pET28a(+) vector as described elsewhere (*30*). The protein was expressed as an amino terminal 6-His tag fusion protein in BL21 DE3 *E. coli* cells. The cells were grown in 250 mL of LB medium in the presence of 30 μg/mL kanamycin and induced at OD_{600nm} of 0.6−0.8 with 1 mM IPTG. Harvesting and protein purification was done as described above with the only exception being that the lysis buffer did not contain any protease inhibitors. A 1.5 mL bed volume of Ni beads was used for immobilizing the protein. Pure His-tag cleaved CERMAD was obtained by mixing the CERMAD loaded Ni beads with a batch of 3c protease loaded Ni beads for 5−6 h, followed by subsequent collection of the cut protein. The pure, untagged CERMAD was then dialyzed into the desired buffer (SnakeSkinT dialysis tubing, 3.5K MWCO, Pierce Biotechnology Inc.) and concentrated to 0.4 mM for ITC studies (Amicon Ultra-15 centrifugal filter devices, 5K MWCO, Millipore) or combined with FERM for the formation of the N/C complex for NMR studies.

The FERM gene (aa, 1−297) in a pQE16 expression vector (a gift from Professor Anthony Bretscher, Molecular Biology and Genetics, Cornell University, Ithaca, NY) was expressed in BL21 DE3 *E. coli* cells. The cells were grown in 1 L of LB medium in the presence of 100 μg/mL ampicillin at 37 °C prior to induction. After induction with 1 mM IPTG at OD_{600nm} of 0.9, the cells were grown at 25 °C for 4 h and harvested as described above. All purification steps were carried out at 4 °C. The cells were lysed in 20 mL of buffer C (200 mM KH_2PO_4 at pH 7.0), supplemented with 20 μL of PI cocktail and 1 mg/mL lysozyme. The lysed cells were sonicated and cleared by centrifugation at 11,000*g* for 40 min. The cleared supernatant was filtered and loaded onto a 5 mL bed volume hydroxyl apatite column (Macroprep Ceramic Hydroxyapatite Type I 80 μm, Biorad) equilibrated in buffer C. The column was washed in 20 bed volumes of the same buffer. Pure FERM was eluted from the column using 10 mL of 0.6 M KH_2PO_4 at pH 7.0 and dialyzed (SnakeSkinT dialysis tubing, 3.5K MWCO, Pierce Biotechnology Inc.) into the desired buffer for ITC studies.

The N/C complex was formed by adding purified CERMAD dialyzed into buffer C (SnakeSkinT dialysis tubing, 3.5K MWCO, Pierce Biotechnology Inc.), to FERM immobilized on a hydroxyl apatite column. After a 10 bed volume wash in buffer C, the complex was eluted in 12 mL of 0.4 M KH_2PO_4 at pH 7.0, dialyzed (SnakeSkinT dialysis tubing, 3.5K MWCO, Pierce Biotechnology Inc.) into the NMR buffer (Walpole's acetate at pH 5.6, 5 mM DTT, 0.1% sodium azide, and 0.1% v/v PI cocktail, Sigma), and concentrated to ∼0.5 mM (Amicon Ultra-15 centrifugal filter devices, 10K MWCO, Millipore) for NMR studies. This method of purification ensures excess FERM since free CERMAD passes through the column during column washes.

NMR Experiments for Structure Verification. TROSY versions of the HNCO, CT-HNCA, HNCACB, and HNCOCA triple resonance experiments (implemented in Biopack, Varian Inc.) were run on an {$^{15}N/^{13}C$} and >90% deuterated CERMAD/natural abundance FERM complex in a Varian Inova 600 MHz spectrometer at 30 °C to obtain chemical shift assignments for structural analysis. ^{15}N-edited NOESY experiments (80 ms, 100 ms, and 150 ms mixing times) were run on an {$^{15}N/^{2}H$}-CERMAD/natural abundance FERM sample to obtain through-space connectivities. All spectra were processed using NMRPipe/NMRDraw (*31*) and analyzed using Sparky (*32*). Chemical-shift values were referenced using DSS as described in detail elsewhere (*33*, *34*).

Table 1: Predicted NOE cross-peaks from the Homology Model

H_N (CERMAD)	structural element	group	approximate distance (Å)	ambiguous?	observed?
T497	β strand	Hγ, Hδ of L273	4.06, 3.45	no	no
T 497	β strand	Hβ of D251	4.24	no	no
T497	β strand	ring protons of F249	4.45	no	no
R517	3_{10}	Hβ of Y565	3.94	no	no
E520	α	Hβ of D196	2.70	yes	no
L531	αA	Hδ of L123	4.37	yes	no
L534	αA	ring protons of W174	3.68, 4.03	no	no
R542	Loop	Hδ of H160	3.82	no	no
H554	αB	Hδ of L233	4.25	yes	no
K564	αC	Hγ of T519	4.67	no	no
K564	αC	Hγ of E198	4.78	yes	no
R569	αC	Hβ, Hγ of E515	4.67,4.56	yes	no
I580	αD	ring protons of F239	3.81, 4.11	no	yes
E582	αD	Hδ of I237	4.58	no	no
F583	αD	Hδ of I237	3.19	no	yes

Isothermal Titration Calorimetry. Both FERM (~3 mL) and CERMAD (~300 μL) were dialyzed (Slide-A-Lyzer 3.5 MWCO Dialysis Cassettes, Pierce Biotechnology Inc.) for 12−18 h into the same buffer bath (2 L volume). Measurements were made in three different buffers of the same ionic strength at pH 7.0 and in acetate buffer at pH 6.0. The solutions used were 100 mM sodium acetate (pH adjusted using glacial acetic acid), 100 mM MES (pH adjusted using 10 M NaOH), and phosphate buffer (17.4 mM KH_2PO_4 and 27 mM $Na_2HPO_4{\cdot}2H_2O$ at pH 7.0). All samples were degassed for 10 min prior to use, and all measurements were carried out in duplicate. ITC experiments were run in a Calorimetry Sciences Corp. (Lindon, UT) Nano-ITC Series III instrument at 25 °C. The reaction cell was filled with ~1.4 mL of 10 μM FERM, and CERMAD (0.2 mM) was titrated into the cell in 25 injections of 4 μL each, with constant stirring at 150−200 rpm throughout the experiment and 240 s between each injection. The heat of ligand dilution was obtained from the average heat of the last few injections after complete saturation of FERM. This value was subtracted from all of the injection points during data analysis.

All data were fit to a single site binding model (*35*) using Bindworks (version 3.1.5, Calorimetry Sciences Corp. Lindon, UT) to yield the stoichiometry (n), association constant (K_a) and observed enthalpy change (ΔH_o) for the binding reaction. The number of protons (N) gained (positive N) or released into the buffer (negative N) upon formation of the protein complex was obtained from the observed enthalpy change (ΔH_o) measured at the same pH and ionic strength using two buffers with different ionization enthalpies (ΔH_b). The ionization enthalpy of a given buffer corresponds to the enthalpy change associated with the release of a proton from the buffer (*36*, *37*). Using the fundamental relationship $\Delta H_o = \Delta H_i + N \times \Delta H_b$, a plot of ΔH_o versus ΔH_b yields a straight line with N as the slope and ΔH_i as the y-axis intercept (*36*). For this purpose, ITC measurements were obtained in both MES ($\Delta H_b^{MES} = 3.71 \pm 0.01$ kcal/mol, (*37*)) and Phosphate ($\Delta H_b^{Phos} = 1.22 \pm 0.01$ kcal/mol, (*37*)) buffers at pH 7.0, 25 °C, and an ionic strength of 0.1. The free energy change (ΔG) and the entropy change (ΔS) for the binding reaction were obtained from the fundamental relationships $\Delta G = -RT \ln K_a$ and $T\Delta S = \Delta H_i - \Delta G$, where R is the universal gas constant (1.986 cal $K^{-1}mol^{-1}$), and T is the absolute temperature.

Hydrogen−Deuterium Exchange (HX). All HX experiments were run with {$^{15}N/^{2}H$}-CERMAD/natural abundance FERM samples in acetate. HX data was collected at pH values of 5.8, 6.0, 6.45, and 7.0. For pH values ≥6.0 (beyond the buffering capacity of acetate), the protein was exchanged into a deuterium-based solution containing 100 mM sodium acetate (deuterated) with pH adjusted to the desired value using glacial acetic acid (deuterated). pH measurements were made using an ISFET stainless steel pH probe (IQ Scientific Instruments) and used without any correction. Sample pH was measured after the completion of data collection. The protein in water-based buffer was rapidly exchanged into the deuterated buffer using Zeba desalting columns (Pierce Biotechnology Inc.). There was typically a 7−9 min lag time between the start of exchange and initiation of data collection. ^{1}H-^{15}N HSQC spectra were collected over a period of 4−7 days depending on the remaining signal. The first four HSQCs were each collected for 40 min (with 16 transients and 64 increments). The number of transients (*nt*) was progressively increased for later time points. Peak volumes were extracted using the nonlinear spectral line shape modeling program, nlinLS (Frank Delaglio, NIH/NIDDK), scaled appropriately to account for the different *nt* values and fit to an exponential decay to obtain the observed exchange rate constant, k_{ex}. The time since exchange was taken as the midpoint of each experiment. The intrinsic exchange rate k_{int} for each residue of CERMAD was calculated, taking into account temperature at pH and salt conditions (see Table 1 in Supporting Information) (*38*).

RESULTS

Backbone Resonance Assignments of Bound CERMAD. The solubility of the Ezrin N/C complex was found to be the highest in acetate buffer (100 mM acetate at pH 5.6, 5 mM DTT, 0.1% sodium azide, and 0.1% v/v Protease Inhibitor Cocktail, Sigma). All NMR experiments were performed on Ezrin N/C complex samples in this buffer. Because of the large size of the N/C complex (~50 kDa), {$^{15}N/^{2}H$}- or {$^{15}N/^{13}C/^{2}H$ }-CERMAD/(natural abundance) FERM complex samples were used to run all NMR experiments. Backbone resonance assignments have been completed for 101 out of 108 residues (excluding prolines) with H484, A501, S504, R509, N513, E515, and R529 remaining unassigned. The assignments have been deposited

in the BioMagResBank (accession number 7161) and are reported elsewhere (*39*).

Formation of the N/C Complex Coincides with CERMAD Folding. A comparison of the ^{1}H-^{15}N HSQC spectra of {^{15}N/^{2}H} CERMAD in the absence and presence of excess FERM clearly indicates that free CERMAD is predominantly unstructured with poor chemical-shift dispersion (Figure 1b). Conversely, bound CERMAD is well structured except for the first ~18 residues, which are disordered based on their sharp peaks, clustered toward the center of the spectrum. The corresponding region in Moesin CERMAD was also poorly ordered in the Moesin crystal structures (*17*, *18*). CERMAD in the absence of FERM is known to be very sensitive to proteolytic cleavage, and it has been suggested that free CERMAD cannot adopt the same fold as that observed in the Moesin N/C crystal structure (*17*, *18*). The lack of stable structure in free CERMAD rationalizes its sensitivity to proteolysis and demonstrates that the formation of the N/C complex involves the folding of CERMAD. An alternate purification protocol yielding the complex with excess {^{15}N/^{2}H}-CERMAD yields ^{1}H-^{15}N HSQC spectra with distinct populations for free and bound CERMAD, indicating that these two populations are in slow exchange (data not shown).

NMR Data Is Consistent with the Homology Model. Chemical shifts and NOEs were used to assess the validity of the homology model constructed as described above. The C^α and C' chemical-shift indices (*40*, *41*), calculated using the CSI program (PENCE/CIHR-Group, Joint Software Centre, University of Alberta) (*42*), confirm all five major secondary structural elements of CERMAD and indicate that the first 20 residues are predominantly random coil except for a short stretch of β-strand in the beginning of CERMAD (477−481) (Figure 2a). On the basis of the recent structure of full-length Moesin (*18*), these residues (disordered in the crystal structure) could potentially extend the β sheet of either the F3 or the F1 subdomains of FERM. Sequential d_{nn} values were observed for all four major α helices, further validating the homology model (Figure 2b). NOE cross-peaks to protons on FERM can verify the packing of CERMAD on the FERM surface, but such interdomain cross-peaks were very limited because of the deuteration of CERMAD, which left only exchangeable protons (primarily backbone H^Ns) for NOE observations. On the basis of the Ezrin N/C homology model, a total of 15 NOEs between CERMAD backbone H^Ns and FERM protons are predicted (Table 1). Of these, 5 were ambiguous (intraresidue or sequential CERMAD resonances fall within the expected range of FERM proton chemical shift), and H^Ns not in αC or αD are expected to be weakened because of low stability (see below). Of the remaining, only 2 are within a distance of 4.0 Å and were indeed observed (Figure 2c). Finally, a plot of CERMAD amide proton chemical shift versus homology model-derived H-bond length displays the expected correlation (*43*, *44*), further supporting the homology model (Figure 2d). Thus, multiple forms of NMR data are fully consistent with the homology model, with CERMAD secondary structure confirmed by CSI, short-range NOEs, and the correlation between hydrogen bond length and amide proton chemical shift, and the N/C interface supported by two long-range interdomain NOEs observed in the most stable region of the complex.

Enthalpy-Dominated Nanomolar Affinity of the N/C Complex Does Not Involve a Net Gain or Loss of Protons. A macroscopic perspective on the thermodynamics of binding of CERMAD to FERM was obtained through ITC measurements. The resulting isotherms were fit well by single-site binding curves (Figure 3a) and yielded the expected stoichiometry of 1 (Table 2). The ΔH_o values obtained in MES ($\Delta H_b^{MES} = 3.71 \pm 0.01$ kcal/mol, (*37*)) and phosphate buffers ($\Delta H_b^{Phos} = 1.22 \pm 0.01$ kcal/mol, (*37*)) at pH 7.0 were essentially equal (-26.5 ± 0.5 kcal/mol), as were the association constants ($K_a = (5.70 \pm 0.16) \times 10^6$ M^{-1}), indicating that no net protonation/deprotonation accompanies binding (i.e., $N = 0$, $\Delta H_o = \Delta H_i$) under these conditions (Table 2). These ITC results further show that formation of the N/C complex is in the nanomolar range of affinity ($K_d = 1/K_a =$ 175 nM) and is driven by a large favorable change in enthalpy that outweighs an unfavorable loss of entropy.

N/C Complex Affinity Is Significantly Enhanced in 100 mM Acetate. For comparison of macroscopic thermodynamic parameters with the residue-specific stabilities obtained by NMR, ITC measurements were also made in 100 mM acetate at pH 6.0 and 7.0 (Table 2). Surprisingly, the measured affinity at pH 7.0 ($K_d = 20$ nM) was nearly 9-fold stronger than the affinity in MES and phosphate at the same pH, with a larger favorable change in enthalpy (-34.6 ± 0.5 kcal/mol) and a larger unfavorable change in entropy ($-24.1 \pm$ 0.4 kcal/mol) (Figure 3b and Table 2). Although lowering the pH to 6.0 significantly altered ΔH and $T\Delta S$ ($\Delta\Delta H =$ −2.4 kcal/mol, $\Delta(T\Delta S) = -2.7$ kcal/mol), enthalpy/entropy compensation resulted in only a marginal decrease in affinity ($K_d = 32.1 \pm 0.6$ nM; $\Delta\Delta G = +0.3$ kcal/mol). Notably, the effects of protonation/deprotonation event(s) accompanying binding in acetate would be minimal because of its very small intrinsic heat of ionization ($\Delta H_b = 0.12 \pm 0.01$ kcal/mol, (*37*)).

Hydrogen Exchange Measurements Reveal Variation in Stability across CERMAD Secondary Structural Elements in the N/C Complex. An amide proton in a protein exists in equilibrium between the closed or exchange-incompetent state (NH_{cl}) and the open or exchange-competent state (NH_{op}), governed by the opening and closing rate constants, k_{op} and k_{cl}, respectively (*45*). The interpretation of k_{ex} values depends on the exchange mechanism (EX1 or EX2) displayed by each amide proton, which in turn is dictated by the relative magnitudes of k_{int} and k_{cl} (*46*). In the EX2 condition ($k_{int} \ll k_{cl}$), the ratio of k_{int} to k_{ex} yields a protection factor (P) which can be translated into apparent free energy of opening, ΔG_{open}. In the EX1 condition ($k_{int} \gg k_{cl}$), k_{ex} directly reports the k_{op} for that amide proton (*46*).

HX data was collected at four different pH values (5.8, 6.0, 6.45, and 7.0) in 100 mM sodium acetate (Table 3). At pH 5.8, the first 40 min HSQC spectrum showed 35 peaks corresponding to protected residues (Figure 4a), and 9 of these remained significantly above the noise level after 106 h of data collection. Seven of the above nine peaks mapped to αD of CERMAD in the homology model and the remaining two to αC. Of the 35 protected peaks, 28 yielded sufficient data for the determination of k_{ex} values, providing quantitative representation of all secondary structural elements except for the β-strand, which exchanged too rapidly (Table 3). As expected, all 35 protected residues are hydrogen bonded in the homology model. Amide protons of residues

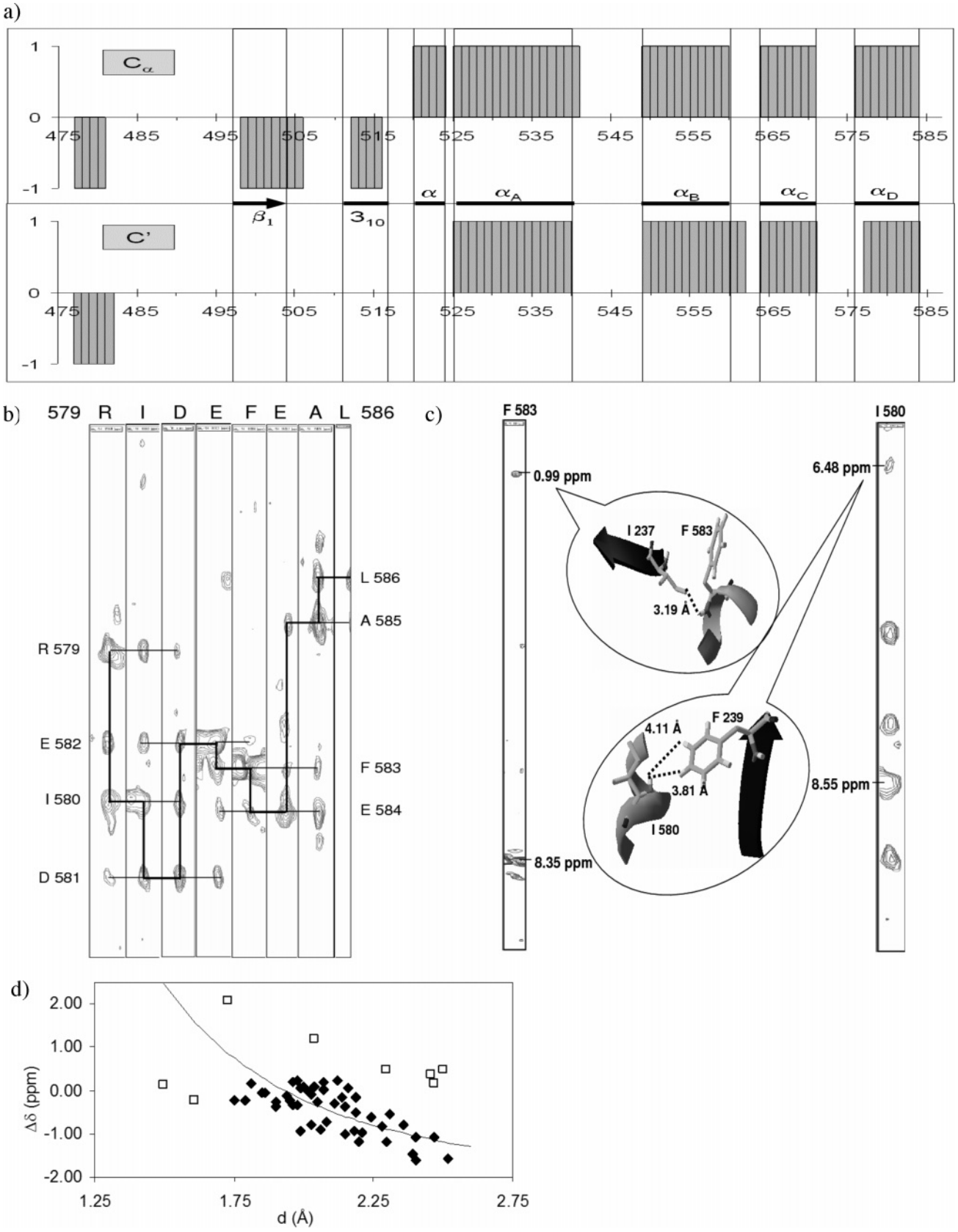

FIGURE 2: Consistency of homology model with NMR data. (a) Filtered C_α and C′ chemical shift indices, calculated using the CSI program (PENCE/CIHR-Group, Joint Software Centre, University of Alberta). Secondary structure from the homology model is indicated between the plots for C_α and C′. The β-strand is not detected in the C′ filtered CSI because of the lack to complete assignments. (b) Example of a series of NOESY strips showing sequential connectivity in αD. (c) NOESY strips showing cross-peaks to FERM residues across the interface. (d) Plot showing correlation between isotropic amide proton chemical shift and hydrogen bond length. The difference between the observed chemical shift and random coil values ($\Delta\delta$ ppm) (*94*) is plotted against the hydrogen bond length, *d* Å (distance between amide proton and carbonyl oxygen). The best fit line through the filled diamonds represents a d^{-3} dependence of $\Delta\delta$ (*45*). The open squares indicate outliers whose anomalous behavior can be explained by ring current shifts and/or the presence of local positive or negative charges.

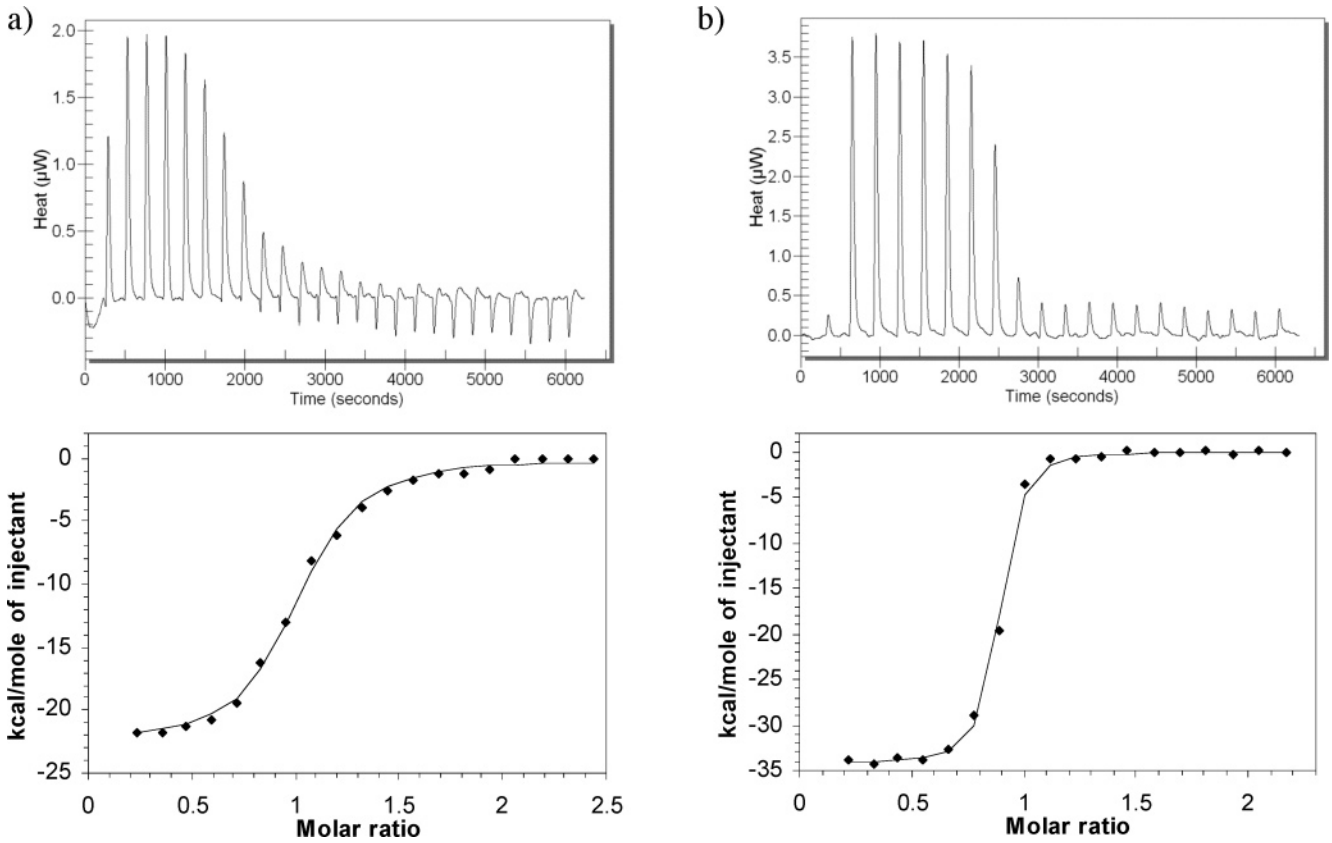

FIGURE 3: Representative ITC raw data (top panels) and integrated heats and data fits (bottom panels) for the titration of 0.2 mM CERMAD into 10 μM FERM in (a) 100 mM MES at pH 7.0 and (b) 100 mM sodium acetate at pH 7.0.

Table 2: Summary of ITC Results for the Titration of 0.2 mM CERMAD into 10 μM FERM[a]

		pH 7.0		pH 6.0
parameter	MES	phosphate	acetate	acetate
n, stoichiometry	0.91 ± 0.05	0.93 ± 0.02	0.91 ± 0.07	1.03 ± 0.02
K_a ($\times 10^7$ M^{-1})	0.57 ± 0.01	0.57 ± 0.03	5.0 ± 0.7	3.1 ± 0.06
K_d (nM)	175 ± 3	176 ± 9	20 ± 3	32.1 ± 0.6
ΔG (kcal/mol)	-9.21 ± 0.01	-9.20 ± 0.04	-10.5 ± 0.1	-10.2 ± 0.1
ΔH (kcal/mol)	-26.8 ± 0.2	-26.2 ± 0.12	-34.6 ± 0.5	-37.0 ± 0.3
$T\Delta S$ (kcal/mol)	-17.8 ± 0.01	-17.0 ± 0.09	-24.1 ± 0.4	-26.8 ± 0.2

[a] The results reported are (average $\pm$ standard deviation) of two independent measurements.

in the first turn of each helix showed no protection since they do not participate in the regular hydrogen bonding of the helix backbone. One exception is V527, the third residue of αA, which is hydrogen bonded to the side chain of N524 in the homology model and showed quantifiable protection.

Protection Factors Indicate a Range in Stability across the Five Main Secondary Structural Elements of CERMAD. Residues in β1 and αB are the least protected, indicating that these regions are significantly more dynamic than the other three helices (Figure 5). Notably, most of the residues of αB have high k_{int} values, making quantitative HX measurements more difficult. Helices αC and αD are the most protected and show relatively uniform ln(*P*) values across the hydrogen-bonding network of each helix, indicating cooperative unfolding. While the individual errors in ln(*P*) are much smaller than the standard deviation of these values within each helix, it should be noted that errors in k_{int} values have not been considered. In contrast, residues of αA display a periodic variation in protection, with residues on the face packed against FERM (e.g., Q528 and L531) more protected than those on the solvent accessible face (e.g., Q530, T533, and S536) (Figure 6). Helix αA is the longest helix of CERMAD and is curved, with longer and weaker hydrogen bonds on the outer convex surface (e.g., S536 with a hydrogen bond length of 2.36 Å) than in the packed concave surface (e.g., S535 with a hydrogen bond length of 1.99 Å). Other such helices with similar protection patterns have been observed in coiled coil leucine zippers (*47*) and surface helices of *trp*-repressor (*48*). Notably, the HX-derived ΔG_{open} values across CERMAD are all less than ΔG_{ITC} (except for L586, discussed below), indicating that exchange occurs predominantly via local fluctuations.

Residues of αC and αD Show Reduced Stability below pH 7.0. In order to identify the appropriate exchange mechanism (EX1 or EX2) for protected residues, plots of log k_{ex} vs log k_{int} were generated. When protein stability is unperturbed by pH, a slope of 1 in this plot indicates EX2 exchange and a slope of 0, EX1 exchange (*49*, *50*). It is possible for different residues within a given protein to exhibit different exchange regimes, as has been observed for example in the Lac headpiece bound to DNA (*51*). F583 is not considered in the set of residues from αD because it

Table 3: Observed Exchange Rates for Protected Residues on CERMAD Bound to FERM at the Four pH Conditions in 100 mM Sodium Acetate[a]

structural element	residue	k_{ex} ($\times 10^{-4}$ min^{-1})[b,c,d] pH 5.8	pH 6.0	pH 6.45	pH 7.0	slope (log k_{ex} vs log k_{int})
β strand	Y499	P	P	-	-	
α	T519	P	P	-	-	
α	E520	P	P	-	-	
α	A 521	241 ± 52	-	-	-	
α	E 522	81.3 ± 4.87	-	-	-	
α	K523	P	P	P	-	
αA	V 527	18.6 ± 1.93	24.9 ± 4.39	59.6 ± 16.3	60.6 ± 17.2	0.52 ± 0.11
αA	Q 528	6.5 ± 0.27	6.8 ± 1.57	19.4 ± 3.84	63.6 ± 5.45	0.86 ± 0.04
αA	Q530	P	P	P	-	
αA	L 531	3.57 ± 0.14	3.59 ± 0.59	6.74 ± 0.57	22.8 ± 2.9	0.60 ± 0.04
αA	L 532	11.5 ± 0.42	9.67 ± 1.87	10.3 ± 1.1	17 ± 4.27	0.01 ± 0.06
αA	T533	P	P	-	-	
αA	L 534	12.7 ± 0.34	11.6 ± 1.83	20.6 ± 2.2	39.7 ± 12.9	0.36 ± 0.07
αA	S 535	48.6 ± 6.23	57.3 ± 11.6	50 ± 12.9	P	0.03 ± 0.21
αA	E 537	28.4 ± 5.81	57.3 ± 21.8	P	P	
αA	L 538	346 ± 12.4	103 ± 28	P	-	
αB	D551	P	P	-	-	
αB	I 552	82.6 ± 13.6	57.9 ± 8.9	-	-	
αB	I 553	46.9 ± 11	36.6 ± 23.7	P	-	
αC	T 567	17.8 ± 2.62	32 ± 8.33	122 ± 50.6	P	1.42 ± 0.31
αC	L 568	1.83 ± 0.16	2.22 ± 0.48	4.35 ± 0.74	6.75 ± 3.74	0.43 ± 0.12
αC	R 569	4.68 ± 0.17	4 ± 0.72	8.24 ± 0.6	23 ± 3.49	0.50 ± 0.04
αC	Q 570	40.1 ± 5.04	41.1 ± 10.7	P	P	
αC	I 571	2.6 ± 0.14	2.18 ± 0.41	5.74 ± 0.74	7.63 ± 0.61	0.42 ± 0.04
αC	R 572	8.45 ± 0.65	10.3 ± 2.29	11.3 ± 1.69	30.1 ± 9.73	0.29 ± 0.09
αC	Q573	P	-	-	-	
αD	Q578	P	P	P	-	
αD	R 579	14.4 ± 0.37	14.9 ± 2.95	81.8 ± 7.99	216 ± 42.1	1.14 ± 0.05
αD	I 580	0.93 ± 0.08	1.86 ± 0.21	3.2 ± 0.16	6.15 ± 0.59	0.69 ± 0.04
αD	D 581	0.92 ± 0.05	1.44 ± 0.07	1.7 ± 0.13	2.44 ± 0.16	0.32 ± 0.03
αD	E 582	0.98 ± 0.03	1.18 ± 0.07	1.27 ± 0.09	1.56 ± 0.09	0.17 ± 0.02
αD	F 583	0.37 ± 0.06	0.5 ± 0.09			
αD	E 584	1.8 ± 0.04	1.66 ± 0.18	2.82 ± 0.12	4.86 ± 0.35	0.36 ± 0.02
αD	A 585	1.95 ± 0.05	1.8 ± 0.16	2.8 ± 0.16	4.38 ± 0.39	0.29 ± 0.03
αD	L 586					

[a] Errors in the rates are standard errors of the fit. Also presented are the slopes of log k_{ex} vs log k_{int} for residues with quantifiable exchange in at least 3 pH conditions. [b] P indicates protection only in the first one or two spectra. (Exchange rates could not be calculated.) [c] (-) indicates that the residue was not protected at that pH. [d] Blanks indicate that exchange rates could not be calculated because of the lack of significant decay in peak volumes.

does not decay significantly at pH 6.45 and 7.0; therefore, exchange rates could not be obtained. Residues I580-E582, E584, and A585 of αD exhibited a slope of 0.37 (±0.06) and residues L568-R572 of αC a slope of 0.41 (±0.13) (Figure 7a and b). Both sets of residues within each element significantly deviate from EX1 or EX2 kinetics (i.e., the slope is neither 0 nor 1) but display slopes within uncertainty of each other. Three scenarios can be considered to explain this deviation, where these residues in αC and αD (1) are in EX2 limit, but their stability decreases below pH 7.0; (2) transition from EX2 to EX1 kinetics as pH is increased; and (3) are in EX1 limit, but their stability increases below pH 7.0.

As presented above, ITC results indicate that $|\Delta G_{bind}|$ is in fact ~0.3 kcal/mol lower at pH 6.0 than at pH 7.0, corresponding to higher affinity at pH 7.0 (i.e., a decrease in complex stability below pH 7.0). The deviation of the above slopes from unity corresponds to a ~0.5 kcal/mol increase in stability for αD (*RT* ln(slope)) and a ~0.3 kcal/mol increase in stability for αC in going from pH 5.8 to pH 7.0, in excellent agreement with the ITC-derived stability increase. Furthermore, despite different k_{int} and k_{ex} values, the ΔG_{open} calculated for these residues at pH 7.0 (assuming EX2) are within 0.5 kcal/mol of each other (Table 4 illustrates this for αD), which is the typical uncertainty for ΔG_{open}, after considering errors in both k_{int} and k_{ex} (*52*). These results support scenario 1 above, where αC and αD together form a cooperative unit of folding, residues within these helices display EX2 kinetics, and their stability decreases below physiological pH.

L586 and F583 Are the Anchors of αD. The C-terminal residue L586, the most protected residue in CERMAD, showed no significant decay with time preventing the determination of an exchange rate. However, if the ITC-derived K_a at pH 6.0 and pH 7.0 is applied, then the observed HX intensity decays for this residue fall very close to the calculated curves (Figure 4b), indicating that the exchange behavior of L586 reflects the macroscopic dissociation constant. It should be noted that this comparison of ΔG_{op} with ΔG_{bind} represents a special case in which folding is tightly coupled to binding, as is the case here for the N/C complex. The more general approach for relating HX-derived free energies to global folding thermodynamics relies on the use of a denaturant such as urea with extrapolation back to native (0 M urea) conditions (*53*). F583 also showed no significant decay with time at pH 7.0 and 6.45, but its exchange rate increased at pH values below 6.45, indicating

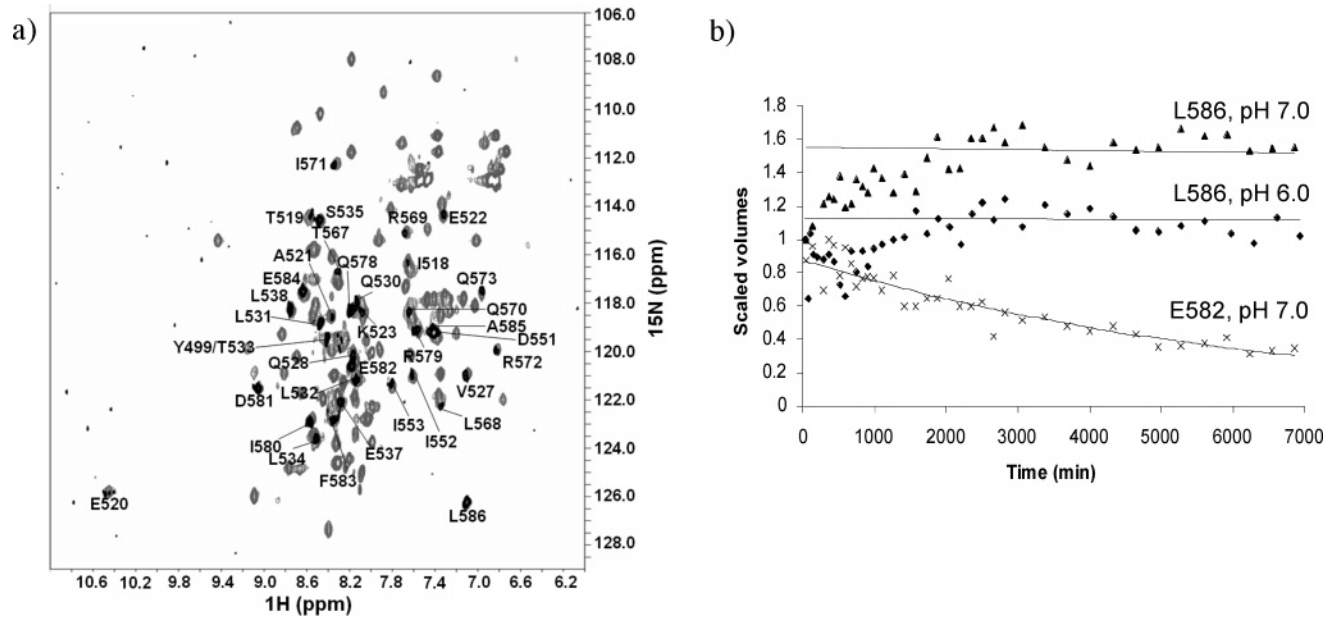

FIGURE 4: (a) HSQC overlay of complex in water (gray) with the first 40 min HSQC of the complex in D_2O (black). The protected residues are labeled. (b) Plot showing the HX profile of L586 at pH 6.0 and pH 7.0 (solid diamonds and solid triangles, respectively) and the theoretical curve for the residue using ITC derived K_a at the respective pH values. Also shown is the decay profile and best fit for a representative residue, E582.

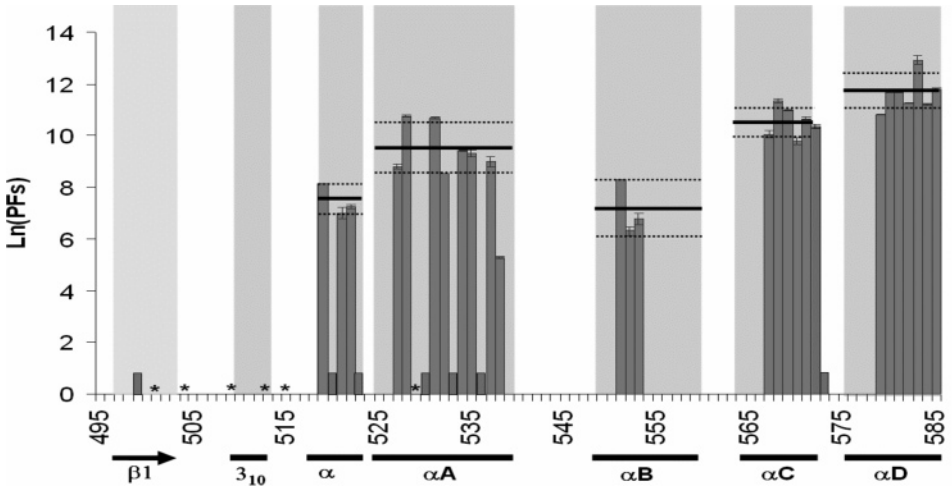

FIGURE 5: Plot of *ln* (protection factors) vs amino acid sequence for CERMAD bound to FERM in acetate buffer at pH 5.8. The secondary structural elements of CERMAD are shown below the sequence and as shaded regions. The shortest bars are for the residues that are protected only in the first spectrum, and therefore, exchange rates could not be determined for these. The residues marked with * could not be assigned. The average protections (as solid lines) and the standard deviations (as dotted lines) are also shown for each secondary structural element. Unprotected/poorly protected residues were not considered while determining this average. The plot was generated for pH 5.8 since quantifiable data for most residues was obtained at this pH because of lower intrinsic rates at pH 5.8 than pH 7.0.

a reduction in stability at lower pH. This behavior is not explicitly observed for L586 and may be attributed to a counteracting fall in HX rate due to a pH-dependent k_{ex} and reduction in stability at lower pH values. Additionally, the effect of hydrogen exchange would be more visible in F583 than in L586 because of its 1.5-fold higher k_{int}.

Another aspect of the decay profile of L586 is the initial increase in peak volume at all four pH values (Figure 4b). A possible explanation for this is that with progressive replacement of exchangeable protons in the vicinity of L586 with deuterons, the dipolar contribution to the transverse relaxation rates (R_2) of the L586 ^1H_N and ^{15}N nuclei decreases with time, imparting an overall decrease in L586 R_2 with time dictated by the HX rates of the nearby protons. This results in increased peak intensity until all nearby protons are exchanged for deuterons, at which time R_2 stays constant, and the intrinsic decay of L586 predominates. This effect is most pronounced for residues displaying the slowest exchange that have more rapidly exchanged neighboring protons. The L586 proton environment in the homology model suggests that such an effect would be dominated by the ^1H_N of A585, by virtue of its proximity to the L586 ^1H_N (inter-proton distance = 2.41 Å) and its quantifiable k_{ex}.

Fourth Residue of α*A,* α*C, and* α*D Behave Similarly.* Q528, T567, and R579 are the fourth residues (and the first hydrogen bonded residues) of αA, αC, and αD, respectively. All three residues behave differently from the other members of their respective helices and exhibit a slope close to 1 in a plot of log k_{ex} versus log k_{int} (Figure 7c). For EX2 exchange, this indicates that their stability is not affected by pH and

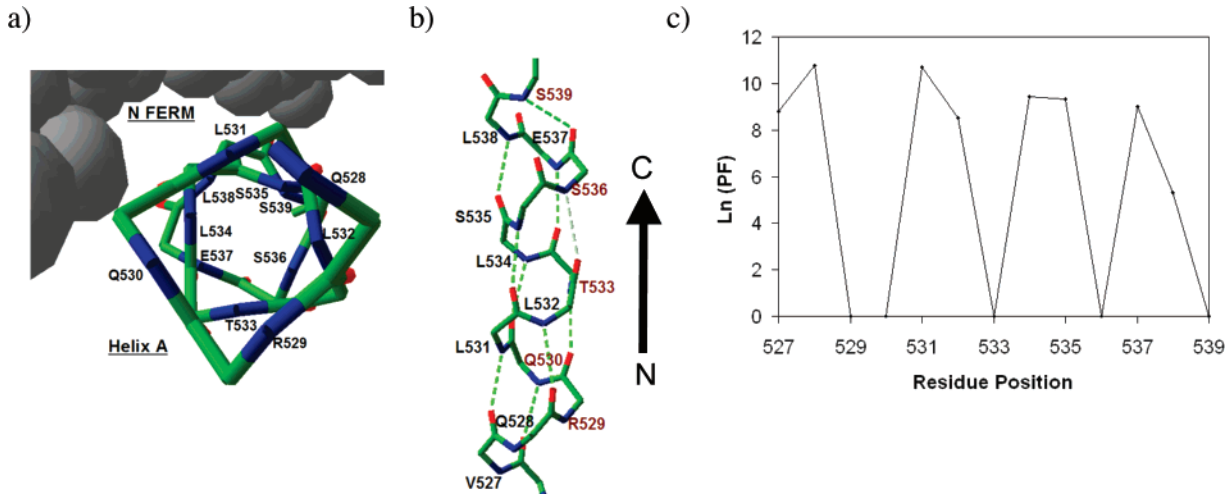

FIGURE 6: Position-dependent protection in αA. (a) Looking down through the αA backbone from the N-terminus to C-terminus bound to the FERM surface (gray). (b) Curved αA, with protected residues on the left (black) and poorly protected residues toward the right (red). (c) Plot highlighting the position-dependent protection in αA.

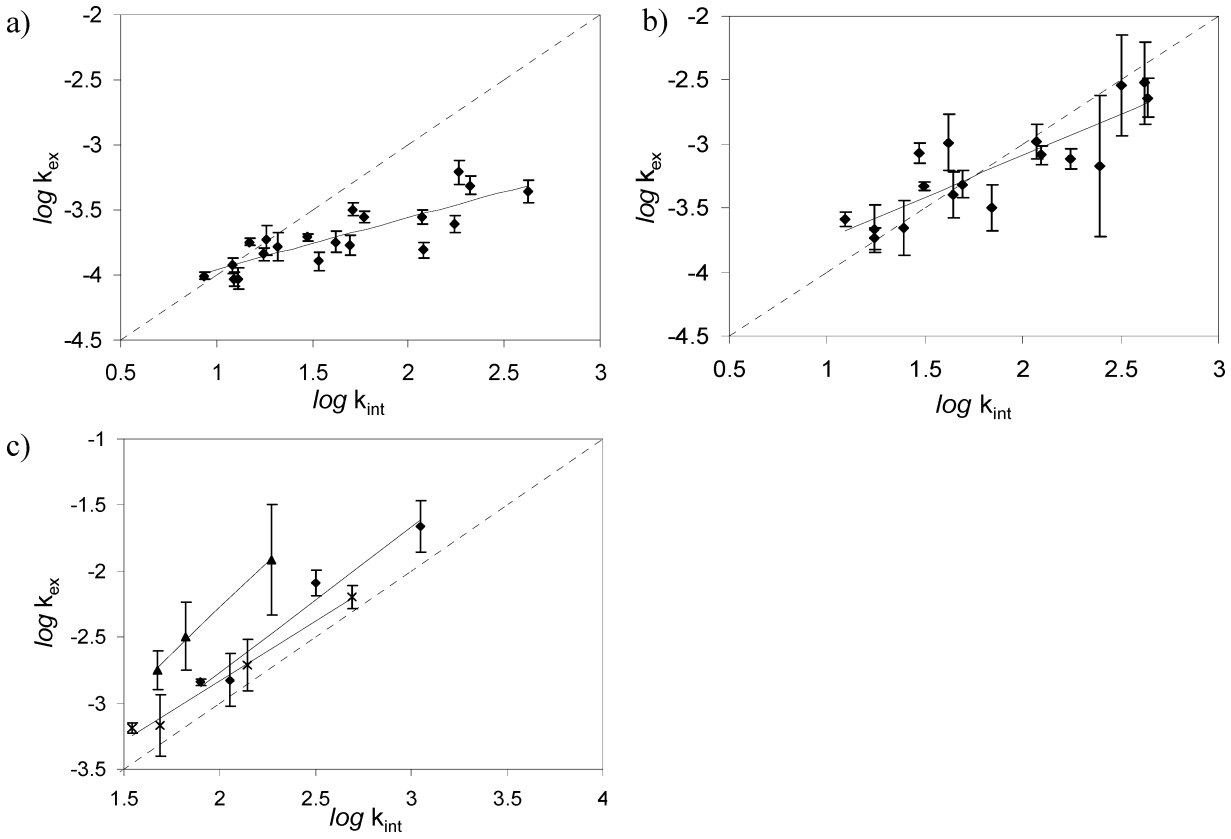

FIGURE 7: log k_{ex} vs log k_{int} plots and their corresponding best fit lines at pH 5.8, 6.0, 6.45, and 7.0 for (a) αD: I580-E582, E584, and A585; (b) αC: L568-R572; (c) Q528 (×), T567 (▲) and R579 (♦). The diagonal in each plot represents a slope of 1.

that they exchange through local fluctuations. This non-cooperative behavior is explained by the fact that the opening/closing of these first hydrogen bonds does not require breakage of additional bonds, as the reorientation of the carbonyl group of residue (i-4) can occur independent of the rest of the helix.

DISCUSSION

The binding interface between the FERM and CERMAD domains of Ezrin displays two highly unusual aspects. First, the structure of CERMAD is composed of a series of five secondary structural elements that pack against FERM but have very few tertiary contacts within CERMAD. The second aspect is the enormous surface area of FERM that is buried (2700 Å) by the binding of the ~100 residue CERMAD domain (*17*). This multicomponent, extensive interface provides the possibility for multiple regulatory mechanisms which can potentially vary in strength if the microscopic affinities of each element differ from one another. Two main questions addressed in this work are (a) do all the secondary structural elements of CERMAD contribute equally to binding, and (b) how is T567, the phoshorylation target on CERMAD that is buried in the X-ray structure, subject to kinase activity?

Table 4: Thermodynamic Hydrogen Exchange Parameters for αD at pH 7.0

residue	k_{int} (min^{-1})	k_{ex} ($\times 10^{-4}$ min^{-1})[a,b]	protection factor P ($\times 10^4$)	ΔG_{open} (kcal/mol)
T 576	1049.71	-	-	-
K577	853.23	-	-	-
Q578	893.45	-	-	-
R579	1124.78	216 ± 42.1	5.21 ± 1.01	6.53 ± 0.12
I580	182.42	6.15 ± 0.59	29.7 ± 2.83	7.58 ± 0.06
D581	174.21	2.44 ± 0.16	71.4 ± 4.65	8.11 ± 0.04
E582	120.52	1.56 ± 0.09	77.3 ± 4.56	8.16 ± 0.04
F583	240.47	*	*	*
E584	209.44	4.86 ± 0.35	43.1 ± 3.09	7.81 ± 0.04
A585	417.90	4.38 ± 0.39	95.4 ± 8.52	8.28 ± 0.05
L 586	155.26	*	*	*

[a] Cells with (-) indicate that the residue was not protected at that pH. Cells with (*) indicate that exchange rates could not be calculated because of the lack of significant decay in peak volumes. [b] The errors reported are standard errors of the fits.

Ezrin N/C interface Is Varied and Dynamic. Our NMR and ITC results clearly demonstrate that binding of CERMAD to the FERM surface is synonymous with folding of CERMAD and that the different CERMAD secondary structural elements range in their stability. The similarity of ΔG_{open} across a given element, yet the variation in microscopic affinities across the different elements (Figure 8d), reveals a highly dynamic interface in which elements form/bind and melt/dissociate independently, providing many combinations of bound elements at a given instant. This is very different from a simple two-state equilibrium where CERMAD might behave as a rigid body composed of stable secondary structural elements that bind and release simultaneously across the FERM binding interface. Rather, the energy landscape is more complex with multiple possible states corresponding to the various combinations of bound secondary structural elements of different affinities. The Ezrin N/C interface provides multiple options for interactions with different regulatory factors, with a possible hierarchy of affinities needed for effective competition depending on which CERMAD element is displaced.

Our ITC results show that binding of CERMAD to FERM is characterized by a favorable ΔH and an unfavorable ΔS. This is atypical for protein−protein binding interactions, although it is quite typical for binding events that involve substantial conformational rearrangement and/or entrapment of water molecules at the binding interface (*54*). Empirical relationships that correlate enthalpy and entropy changes with the apolar and polar surface area buried upon binding (ΔASA_{apolar} and ΔASA_{polar}, respectively) provide estimates of ΔH and ΔS for a given interface (*54*−*57*). These estimates report on the changes accompanying the binding of two preordered surfaces; hence, no changes in conformational entropy are considered. The predicted ΔH thus obtained for the Ezrin N/C interface (−15 kcal/mol) is far less favorable than that observed by ITC (−26.5 kcal/mol in MES/phosphate buffers), consistent with the cooperative formation of secondary structure, side chain packing, and interactions that accompany CERMAD binding, in addition to the extensive interactions across the N/C interface. Similarly, the large discrepancy between the predicted (101 kcal/mol) and measured (−17 kcal/mol) $T\Delta S$ is rationalized by the additional loss of conformational freedom due to folding/binding of the ∼100 residue CERMAD polypeptide. Hence, the relative partitioning of binding energy into enthalpy and entropy is not unexpected for this system, considering the large binding interface and the coupling of binding and folding in CERMAD.

Critical Roles of F583 and L586 in Stabilizing αD. It has been shown that the 11 C-terminal residues of EBP 50, an adapter protein that binds to the active FERM domain, bind in the same site of FERM as αD of CERMAD (*58*, *59*). Moreover, F583 and the hydrophobic nature of the C-terminal CERMAD residue (L or M) are completely conserved across ERM proteins, Merlin and EBP 50 (*58*, *59*). It was previously demonstrated that EBP 50 alone does not displace CERMAD in dormant Ezrin, indicating that the N/C interaction must be weakened in order for this adapter to bind (*11*). Here, we have shown that αD is the tightest binding region of CERMAD and that the HDX-derived stabilities of F583 and L586 reflect the macroscopic binding constant measured by ITC. This indicates that these two residues serve as anchors of αD, and their release from the binding interface coincides with release of the entire CERMAD molecule.

The homology model provides rationalization for this high protection of F583 and L586. Both side chains are packed into a hydrophobic patch on the FERM surface, with the L586 side chain surrounded by L215, I226, and I237 side chains of FERM and the F583 ring. Helix αD terminates in a type I β turn with the L586 amide proton hydrogen bonded to the carbonyl oxygen of F583 (Figure 8a) and the C-terminal carboxylate hydrogen bonded to N210 and T214 of FERM (*17*). The NH group of F583 is on the side of αD packed against FERM. These combined hydrophobic packing and electrostatic interactions serve to limit the solvent accessibility of F583 and L586 NH groups, thus protecting them from exchange.

Interestingly, the F583 ring participates in a network of aromatic ring interactions in the F3 subdomain of FERM containing 6 phenylalanine residues spanning a distance of nearly 22 Å (Figure 8b). Aromatic interactions are believed to contribute to the stability of tertiary and quaternary structure (*60*), thermostability of thermophilic proteins (*60*−*62*), and are known to be important in antibody−antigen interfaces (*63*) and, in general, biomolecular recognition (*64*). Phenylalanine zippers have been implicated in the aggregation process of amyloid fibril formation (*65*, *66*) and the dimerization of APS, a scaffolding protein involved in cellular signaling (*67*). An aromatic interaction pair can contribute −0.6 to −1.3 kcal/mol to protein stability at physiological temperature (*60*). The binding of αD to FERM results in the formation of two new aromatic interaction pairs (F268−F254 and F583−F266) (Table 5). Hence, the stability achieved by binding must rely at least moderately on the presence of this phenylalanine residue. This was indeed observed in a binding study of a 28 residue peptide from the C-terminus of EBP 50 to Radixin FERM domain. Mutation of the F to an A resulted in a 25-fold weaker binding compared to the wild type peptide (*59*).

Keystone Interactions: A Microscopic Perspective. In their structural analysis of the active Ezrin FERM domain, Smith et al. introduced the concept of "keystone interactions" to describe regions of the N/C interface predicted to be the most critical (*26*). The high B factors observed for certain stretches

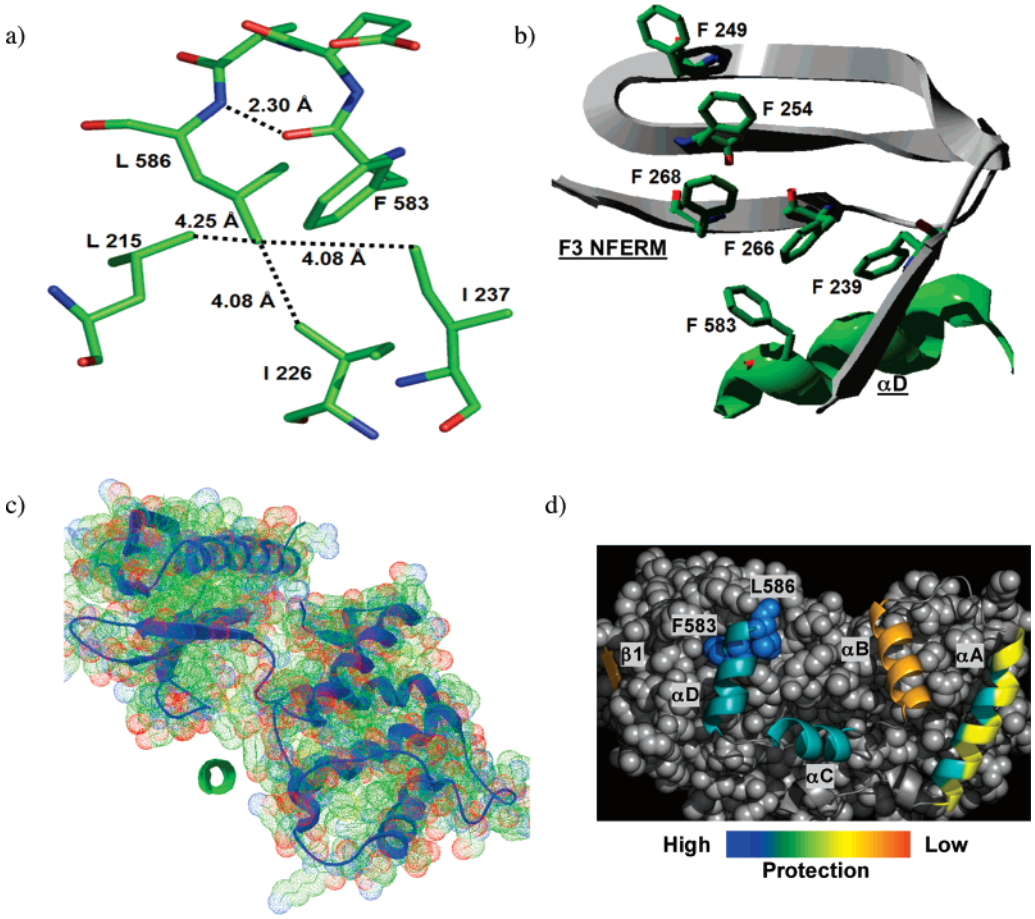

FIGURE 8: (a) L586 NH group, locked into a hydrogen-bonded position to the F583 carbonyl oxygen. (b) Phenylalanine ring network comprising F583 and other phenylalanines from the F3 module of FERM. (c) Looking down through the αB backbone from the N-terminus to C-terminus (green), bound to a cleft between the F2 and F3 modules of FERM. (d) Summary of protection. FERM is shown in the background as a gray space-filled model. The main secondary structural elements of C ERMAD are color coded on the basis of their HX protection.

Table 5: Distance between Centroids of the Phenylalanine Residues That Form a Part of the Phenylalanine Network in the F3 Module of FERM and αD of CERMAD from the Ezrin N/C Complex Homology Model and the Moesin N/C Crystal Structure and the Crystal Structures of the Active FERM Domains of Ezrin and Moesin

		centroid distances (Å)			
		active FERM[b]		dormant FERM	
Group 1[a]	Group 2[a]	Ezrin	Moesin	Ezrin	Moesin
F239	F266	5.51	5.71	4.78	4.81
F266	F268	6.00	6.60	5.76	5.75
F268	F254	10.54	5.15	4.92	4.87
F254	F249	4.77	6.28	6.07	6.08
F239	F574 (F583)			8.13	8.22
F266	F574 (F583)			4.87	4.74
F268	F574 (F583)			7.14	7.21

[a] The residues of Group 1 belong to FERM of Ezrin or Moesin. In Group 2, F 574 belongs to Moesin CERMAD, and F583 belongs to Ezrin CERMAD. [b] The distances are very similar for the dormant complexes between Ezrin and Moesin but vary significantly for the active FERM domains. This might be due to the fact that these residues have been implicated in keystone interactions and hence are very mobile and may be captured in different low-energy conformations.

of residues in the F2 (130−150 and 155−180) and F3 (210−214 and 240−270) subdomains were attributed to the absence of αA and αD, which pack against these regions in the structure of the Moesin N/C complex (*17*). The authors predicted that αA and αD would be the tightest binding regions of CERMAD and that the corresponding regions on FERM would be high-affinity sites for other binding partners. Indeed, high-affinity ligands that bind to the FERM surface masked by αD (EBP50 (*58*), EBP50/NHERF1, and NHERF2 (*59*)) and strand 1 (ICAM-2 (*9*, *68*), CD44, and neutral endopeptidase 24.11 (*9*, *69*, *70*)) have been identified. However, no ligands that bind to the αA-complementary surface have been found, although additional proteins such as RhoGDI (*13*), FAK (*15*), E3KARP (*12*), and PI 3-kinase (*71*) among others are known to interact with Ezrin with the structural details of the interactions yet to be elucidated.

As discussed above, our results clearly demonstrate that αD indeed forms a high-affinity region of the N/C interface. In the homology model, I580, F583, and L586 of αD insert into the core of the F3 residues found to be disordered in active FERM. The disordered F3 region implicated in keystone interactions includes all four Phe residues involved in the aromatic network described above. Hence, in active Ezrin, these Phe residues are likely to sample multiple conformations. Since aromatic interactions depend on both distance and orientation (*60*, *72*, *73*), disorder would diminish their strength. Two aromatic residues are defined to interact if their phenyl ring centroids are less than 7 Å apart (*60*). The introduction of F583 introduces two new aromatic interactions, extending the aromatic network to include a total of six Phe residues (Table 5). The correspondence between

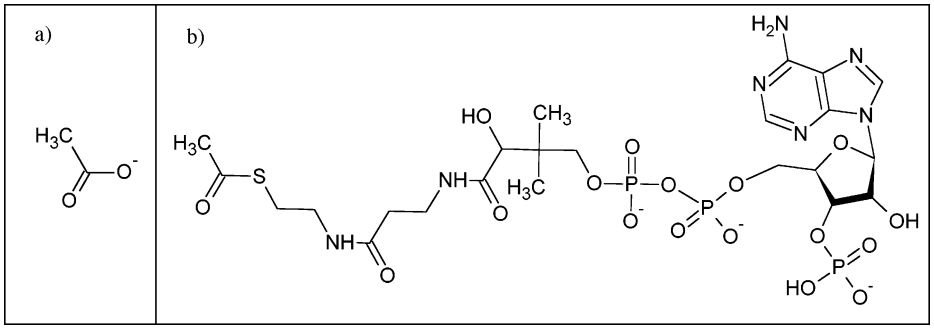

FIGURE 9: Structures of (a) acetate and (b) acetyl coenzyme A (prepared using ChemSketch 10.00, ACD/Labs).

F583 ΔG_{open} and ΔG_{bind} indicates that the Phe−Phe aromatic interaction network formed by the insertion of F583 upon CERMAD binding plays a critical role in the determination of the macroscopic affinity and suggests a mechanism by which conformational perturbations remote from the interaction surface might disrupt this aromatic interaction network and modulate affinity of the N/C interaction. For example, IP3, the soluble head group of PIP2 (which is known to weaken the N/C interaction (*23*)), binds to FERM at the opposite end of this network (*74*).

In contrast, αA residues display a large variation in HX protection factors, an observation attributed to the bending required for packing this long helix against the FERM F2 subdomain surface. This compromise between interface packing and backbone hydrogen bonding renders a lower stability of this helix relative to αD, apparent in the lower protection factors in αA. The highest protection in αA is observed for residues on the packed side of this helix, with values lower than the average protection for αD (Figure 5). The lower stability of αA provides a region of the N/C interface that would be vulnerable to direct competition by regulatory factors with binding affinities that need not be as high as that of the observed affinity of the EBP50 C-terminal peptide for the αD binding site (*59*).

A Possible Ezrin Repression Mechanism Is Suggested by the Thermodynamic Effects of Acetate. Although the macroscopic thermodynamic description of the CERMAD/FERM interaction is easily rationalized, the ~9-fold higher affinity in acetate compared with MES or phosphate buffers at equal ionic strength is unexpected. The more favorable enthalpy and less favorable entropy in acetate compared to MES or phosphate buffers is consistent with further folding-like conformational changes induced by acetate. This might simply be a stabilization of the folded form of CERMAD (i.e., the bound state), or it may reflect an allosteric conformational change in FERM that enhances the affinity of CERMAD through structural ordering and increased electrostatic interactions, possibly induced by specific interaction(s) with acetate.

Interestingly, the F2 subdomain has a fold similar to that of acyl coenzyme A binding protein (*17*) (ACBP) and retains many of the side chains involved in binding acyl-CoA. The increase in N/C affinity observed in 100 mM acetate, a widely used buffer not noted for interacting specifically with proteins, suggests the possible existence of an acetate-like signaling molecule that promotes the repressed state of Ezrin. Acetate presents a fragment of acyl-CoA, mimicking the terminal end of the acyl-fatty acid moiety of acyl-CoA and possibly also providing features similar to those of the carbonyl and aliphatic components of the CoA moiety (Figure 9). A fragment-based approach to drug discovery has recently gained interest, where weak-binding small molecules are linked to form high-affinity bidentate compounds (*75*−*78*). By analogy, the effect of 100 mM acetate on the thermodynamics of the N/C interaction, together with the structural homology of F2 with the Acyl CoA binding domain, suggests an acyl CoA-mediated repression mechanism in Ezrin. Studies are underway in our laboratory to investigate this intriguing possibility.

β1 and αB Provide Possible Fine-Tuning of Active and Dormant Ezrin Populations. Secondary structural elements β1 and αB are the least stable of the five major elements of bound CERMAD. The poor protection of β1 is not unexpected because of the involvement of this element in the domain-swapped dimer in the Moesin N/C complex crystal structure (*17*, *79*). A shallow energy landscape, suggested by the alternate crystal-trapped conformation, is rationalized by the position of β1 as the last strand of a β sheet, where only every-other residue is hydrogen bonded. Helix αB sits in a groove between the F2 and F3 subdomains of FERM (Figure 8c), unlike αC, αD, and αA, which are all bound to one subdomain of FERM (F3 for αC and αD and F2 for αA). Hence, the stability of αB can be easily affected by relative motions of the two subdomains. Also, while the side chains of residues in αC, αD, and αA pack tightly into FERM, only H549, D551, and N557 of αB are within van der Waals contact of the FERM surface and hence provide the primary interactions by which αB is perched on the groove. This loose packing of αB at the N/C interface, however, does not imply that αB is a less significant element in Ezrin function. Notably, CERMAD also binds to f-actin filaments through its C-terminal 34 residues that comprise αB, αC, and αD (*80*), indicating that the region corresponding to αB has an important role in determining CERMAD's f-actin binding ability. The presence of weak elements such as β1 and αB may provide a fine level of control of N/C macroscopic affinity and consequently a fine-tuning of active and dormant Ezrin populations, which can be modulated by upstream signals and downstream effectors.

Activation by Phosphorylation, a Thermodynamic Mechanism? The side chain T567 in αC is inaccessible to solvent and hence to kinases in the X-ray structure (*17*). Hence, the most obvious and intriguing question is how this residue becomes phosphorylated. Our results show that for every ~20,000 molecules (k_{int}/k_{ex}), only one molecule samples the open state at any given time. Therefore, rapid phosphorylation of this residue would not be expected without some perturbation of its local stability. Studies by Fievet et al.

reported that Ezrin activation by phosphorylation at T567 requires phosphoinositide binding to FERM (*81*). This suggests that phosphoinositide binding alters this population ratio, resulting in a higher probability of T567 being accessible to kinase.

Many distributed binding interfaces involving coupled folding and binding have been characterized in higher eukaryotes over the past decade (*82*), with the hallmark feature being the large interaction surface area buried by a relatively short polypeptide chain. Such coupled folding and binding have been found in proteins associated with vital cellular activities such as transcription (the N and C terminal domains of p53 (*83*−*86*), the interaction domains of CBP (cAMP-responsive (CRE)-binding protein) and ACTR (activator for thyroid hormone and retinoid receptors) (*87*)), chromatin structure and gene regulation (HMGA proteins (*88*, *89*)), apoptosis (N terminal domains of DFF40 (DNA Fragmentation Factor) and DFF45 (*90*)), and cell adhesion (E cadherin cytoplasmic domain and its interaction with β catenin (*91*)). Recent pioneering studies on the folding of an unstructured pKID (phosphorylated kinase inducible domain of the transcription factor CREB) upon binding to the KIX domain of CREB binding protein support a mechanism wherein initial nonspecific hydrophobic contacts pave the way for the formation of the final complex held together by a multitude of specific contacts (*92*, *93*). Ligand-coupled folding transitions also play an important role in catalysis in the helicase motor of SecA, an essential component of the bacterial Sec translocase machinery (*94*).

Ezrin, with its extended binding interface serves as a paradigm for this emerging class of proteins. Our approach with the Ezrin interface provides a thermodynamic analysis of the various structural elements of CERMAD that hold FERM and CERMAD together and show that regional affinities and their governing interactions vary across the interface. In all highly evolved, complex signaling networks, proteins typically interact with multiple reversible binding partners. These interactions are tightly controlled by upstream signals and are highly specific. The microscopic thermodynamic variation revealed here for the Ezrin N/C interface may be a typical feature of extended binding interfaces that utilize separate regions of the interface to target different binding partners that modulate the populations of bound and free states.

The critical role of the adapter function of Ezrin has been demonstrated recently in breast cancer metastasis (*6*). Transplantation of a metastatic murine mammary carcinoma cell line overexpressing Ezrin into the mammary fat pad of mice resulted in lung metastases. Impairing the adapter function of Ezrin by overexpressing the FERM domain alone resulted in suppression of this metastasis. Additionally, overexpression of the phosphorylation deficient, adapter function-impaired T567A-Ezrin in a mouse metastatic osteosarcoma cell line completely inhibited metastasis as compared to the same cell line expressing wild type Ezrin (*3*). Both studies highlight the potential therapeutic value of Ezrin repression in controlling metastasis. Our observation of an increase in N/C affinity in acetate suggests a novel mechanism to inhibit the adapter function of Ezrin through promoting this repressed, metastatically incompetent form.

In summary, the above studies have elucidated slow dynamic fluctuations of Ezrin CERMAD at this novel binding interface with FERM. These fluctuations correspond to the independent folding/unfolding equilibria of the individual secondary structural elements of CERMAD. The relative stabilities of the five structural elements of CERMAD indicate that the macroscopic stability of CERMAD is dominated by helices αC and αD, each of which exhibit cooperative behavior. L586 and F583 are the main anchoring residues of CERMAD, with their free energy of opening in agreement with the ITC-derived macroscopic binding thermodynamics. The higher affinity in acetate suggests a potential off switch possibly facilitated through the F2 subdomain with the acyl-CoA binding protein-like fold. The above analysis sets the stage for further studies to elucidate the detailed mechanism of activation and repression at this pathologically significant intra-protein interface.

ACKNOWLEDGMENT

We thank Professor Anthony Bretscher and David Chambers for providing reagents and for helpful discussions on protein purification, Kyriacos Leptos for constructing the 3c protease expression vector, Professor Glyn Stanway, University of Essex, U.K. for providing the HRV-14 viral genome, and Dr. Cynthia Kinsland and the Protein Facility at Cornell University, Ithaca NY, for the use of the Isothermal Titration Calorimeter.

SUPPORTING INFORMATION AVAILABLE

Intrinsic exchange values (k_{int}) for the backbone amide protons of CERMAD at pH 5.8, 6.0, 6.5, and 7.0. This material is available free of charge via the Internet at http://pubs.acs.org.

REFERENCES

1. Bogenrieder, T., and Herlyn, M. (2003) Axis of evil: molecular mechanisms of cancer metastasis, *Oncogene 22*, 6524−6536.
2. Khanna, C., Khan, J., Nguyen, P., Prehn, J., Caylor, J., Yeung, C., Trepel, J., Meltzer, P., and Helman, L. (2001) Metastasis-associated differences in gene expression in a murine model of osteosarcoma, *Cancer Res. 61*, 3750−3759.
3. Khanna, C., Wan, X., Bose, S., Cassaday, R., Olomu, O., Mendoza, A., Yeung, C., Gorlick, R., Hewitt, S. M., and Helman, L. J. (2004) The membrane-cytoskeleton linker ezrin is necessary for osteosarcoma metastasis, *Nat. Med. 10*, 182−186.
4. Yu, Y., Khan, J., Khanna, C., Helman, L., Meltzer, P. S., and Merlino, G. (2004) Expression profiling identifies the cytoskeletal organizer ezrin and the developmental homeoprotein Six-1 as key metastatic regulators, *Nat. Med. 10*, 175−181.
5. Akisawa, N., Nishimori, I., Iwamura, T., Onishi, S., and Hollingsworth, M. A. (1999) High levels of ezrin expressed by human pancreatic adenocarcinoma cell lines with high metastatic potential, *Biochem. Biophys. Res. Commun. 258*, 395−400.
6. Elliott, B. E., Meens, J. A., SenGupta, S. K., Louvard, D., and Arpin, M. (2005) The membrane cytoskeletal crosslinker ezrin is required for metastasis of breast carcinoma cells, *Breast Cancer Res. 7*, R365−R373.
7. Bretscher, A., Chambers, D., Nguyen, R., and Reczek, D. (2000) ERM-Merlin and EBP50 protein families in plasma membrane organization and function, *Annu. Rev. Cell Dev. Biol. 16*, 113−143.
8. Tsukita, S., Oishi, K., Sato, N., Sagara, J., Kawai, A., and Tsukita, S. (1994) ERM family members as molecular linkers between the cell surface glycoprotein CD44 and actin-based cytoskeletons, *J. Cell Biol. 126*, 391−401.
9. Yonemura, S., Hirao, M., Doi, Y., Takahashi, N., Kondo, T., Tsukita, S., and Tsukita, S. (1998) Ezrin/radixin/moesin (ERM) proteins bind to a positively charged amino acid cluster in the juxta-membrane cytoplasmic domain of CD44, CD43, and ICAM-2, *J. Cell Biol. 140*, 885−895.

10. Heiska, L., Alfthan, K., Gronholm, M., Vilja, P., Vaheri, A., and Carpen, O. (1998) Association of ezrin with intercellular adhesion molecule-1 and -2 (ICAM-1 and ICAM-2). Regulation by phosphatidylinositol 4, 5-bisphosphate, *J. Biol. Chem. 273*, 21893−21900.
11. Reczek, D., and Bretscher, A. (1998) The carboxyl-terminal region of EBP50 binds to a site in the amino-terminal domain of ezrin that is masked in the dormant molecule, *J. Biol. Chem. 273*, 18452−18458.
12. Yun, C. H., Lamprecht, G., Forster, D. V., and Sidor, A. (1998) NHE3 kinase A regulatory protein E3KARP binds the epithelial brush border Na+/H+ exchanger NHE3 and the cytoskeletal protein ezrin, *J. Biol. Chem. 273*, 25856−25863.
13. Takahashi, K., Sasaki, T., Mammoto, A., Takaishi, K., Kameyama, T., Tsukita, S., and Takai, Y. (1997) Direct interaction of the Rho GDP dissociation inhibitor with ezrin/radixin/moesin initiates the activation of the Rho small G protein, *J. Biol. Chem. 272*, 23371−23375.
14. Takahashi, K., Sasaki, T., Mammoto, A., Hotta, I., Takaishi, K., Imamura, H., Nakano, K., Kodama, A., and Takai, Y. (1998) Interaction of radixin with Rho small G protein GDP/GTP exchange protein Dbl, *Oncogene 16*, 3279−3284.
15. Poullet, P., Gautreau, A., Kadare, G., Girault, J. A., Louvard, D., and Arpin, M. (2001) Ezrin interacts with focal adhesion kinase and induces its activation independently of cell-matrix adhesion, *J. Biol. Chem. 276*, 37686−37691.
16. Bretscher, A., Edwards, K., and Fehon, R. G. (2002) ERM proteins and merlin: integrators at the cell cortex, *Nat. Rev. Mol. Cell Biol. 3*, 586−599.
17. Pearson, M. A., Reczek, D., Bretscher, A., and Karplus, P. A. (2000) Structure of the ERM protein moesin reveals the FERM domain fold masked by an extended actin binding tail domain, *Cell 101*, 259−270.
18. Li, Q., Nance, M. R., Kulikauskas, R., Nyberg, K., Fehon, R., Karplus, P. A., Bretscher, A., and Tesmer, J. J. (2007) Self-masking in an intact ERM-merlin protein: an active role for the central alpha-helical domain, *J. Mol. Biol. 365*, 1446−1459.
19. Reczek, D., Berryman, M., and Bretscher, A. (1997) Identification of EBP50: A PDZ-containing phosphoprotein that associates with members of the ezrin-radixin-moesin family, *J. Cell Biol. 139*, 169−179.
20. Matsui, T., Maeda, M., Doi, Y., Yonemura, S., Amano, M., Kaibuchi, K., Tsukita, S., and Tsukita, S. (1998) Rho-kinase phosphorylates COOH-terminal threonines of ezrin/radixin/moesin (ERM) proteins and regulates their head-to-tail association, *J. Cell Biol. 140*, 647−657.
21. Nakamura, F., Amieva, M. R., and Furthmayr, H. (1995) Phosphorylation of threonine 558 in the carboxyl-terminal actin-binding domain of moesin by thrombin activation of human platelets, *J. Biol. Chem. 270*, 31377−31385.
22. Simons, P. C., Pietromonaco, S. F., Reczek, D., Bretscher, A., and Elias, L. (1998) C-terminal threonine phosphorylation activates ERM proteins to link the cell's cortical lipid bilayer to the cytoskeleton. *Biochem. Biophys. Res. Commun. 253*, 561−565.
23. Niggli, V., Andreoli, C., Roy, C., and Mangeat, P. (1995) Identification of a phosphatidylinositol-4,5-bisphosphate-binding domain in the N-terminal region of ezrin, *FEBS Lett. 376*, 172−176.
24. Doi, Y., Itoh, M., Yonemura, S., Ishihara, S., Takano, H., Noda, T., and Tsukita, S. (1999) Normal development of mice and unimpaired cell adhesion/cell motility/actin-based cytoskeleton without compensatory up-regulation of ezrin or radixin in moesin gene knockout, *J. Biol. Chem. 274*, 2315−2321.
25. Takeuchi, K., Sato, N., Kasahara, H., Funayama, N., Nagafuchi, A., Yonemura, S., Tsukita, S., and Tsukita, S. (1994) Perturbation of cell adhesion and microvilli formation by antisense oligonucleotides to ERM family members, *J. Cell Biol. 125*, 1371−1384.
26. Smith, W. J., Nassar, N., Bretscher, A., Cerione, R. A., and Karplus, P. A. (2003) Structure of the active N-terminal domain of Ezrin. Conformational and mobility changes identify keystone interactions, *J. Biol. Chem. 278*, 4949−4956.
27. Peitsch, M. (1995) Protein Modeling by E-Mail, *Biotechnology 13*, 658−660.
28. Schwede, T., Kopp, J., Guex, N., and Peitsch, M. C. (2003) SWISS-MODEL: An automated protein homology-modeling server, *Nucleic Acids Res. 31*, 3381−3385.
29. Guex, N. and Peitsch, M. C. (1997) SWISS-MODEL and the Swiss-PdbViewer: an environment for comparative protein modeling, *Electrophoresis 18*, 2714−2723.
30. Walker, P., Leong, L., Ng, P., Tan, S., Waller, S., Murphy, D., and Porter, A. (1994) Efficient and Rapid Affinity Purification of Proteins using Recombinant Fusion Proteases, *Biotechnology (NY) 12*, 601−605.
31. Delaglio, F., Grzesiek, S., Vuister, G. W., Zhu, G., Pfeifer, J., and Bax, A. (1995) NMRPipe: a multidimensional spectral processing system based on UNIX pipes, *J. Biomol. NMR 6*, 277−293.
32. Goddard, T., and Kneller, D. *SPARKY 3*, University of California, San Francisco, CA.
33. Bax, A., and Subramanian, S. (1986) Sensitivity-enhanced two-dimensional heteronuclear shift correlation NMR spectroscopy, *J. Magn. Reson. 67*, 565−569.
34. Live, D. H., Davis, D. G., Agosta, W. C., and Cowburn, D. (1984) Long range hydrogen bond mediated effects inpeptides: Nitrogen=15 NMR studies of gramicidin S in water and organic solvents, *J. Am. Chem. Soc. 106*, 1939−1941.
35. Freire, E., Mayorga, O. L., and Straume, M. (1990) Isothermal titration calorimetry, *Anal. Chem. 62*, 950A−959A.
36. Baker, B. M., and Murphy, K. P. (1996) Evaluation of linked protonation effects in protein binding reactions using isothermal titration calorimetry, *Biophys. J. 71*, 2049−2055.
37. Fukada, H., and Takahashi, K. (1998) Enthalpy and heat capacity changes for the proton dissociation of various buffer components in 0.1 M potassium chloride, *Proteins 33*, 159−166.
38. Bai, Y., Milne, J. S., Mayne, L., and Englander, S. W. (1993) Primary structure effects on peptide group hydrogen exchange, *Proteins 17*, 75−86.
39. Jayaraman, B., and Nicholson, L. K. (2006) Backbone resonance assignments of Ezrin C ERMAD in a non-covalent complex with Ezrin N FERM, *J. Biomol. NMR 36*, 63.
40. Wishart, D. S., Sykes, B. D., and Richards, F. M. (1991) Relationship between nuclear magnetic resonance chemical shift and protein secondary structure, *J. Mol. Biol. 222*, 311−333.
41. Wishart, D. S., Sykes, B. D., and Richards, F. M. (1992) The chemical shift index: a fast and simple method for the assignment of protein secondary structure through NMR spectroscopy, *Biochemistry 31*, 1647−1651.
42. Wishart, D. S., and Sykes, B. D. (1994) The 13C chemical-shift index: a simple method for the identification of protein secondary structure using 13C chemical-shift data, *J. Biomol. NMR 4*, 171−180.
43. Pardi, A., Wagner, G., and Wuthrich, K. (1983) Protein conformation and proton nuclear-magnetic-resonance chemical shifts, *Eur. J. Biochem. 137*, 445−454.
44. Wagner, G., Pardi, A., and Wuthrich, K. (1983) Hydrogen Bond Length and Proton NMR Chemical Shifts in Proteins, *J. Am. Chem. Soc. 105*, 5948−5949.
45. Hvidt, A., and Nielsen, S. O. (1966) Hydrogen exchange in proteins, *Adv. Protein Chem. 21*, 287−386.
46. Bai, Y., Sosnick, T. R., Mayne, L., and Englander, S. W. (1995) Protein folding intermediates: native-state hydrogen exchange, *Science 269*, 192−197.
47. Goodman, E. M., and Kim, P. S. (1991) Periodicity of amide proton exchange rates in a coiled-coil leucine zipper peptide, *Biochemistry 30*, 11615−11620.
48. Finucane, M. D., and Jardetzky, O. (1996) The pH dependence of hydrogen-deuterium exchange in trp repressor: the exchange rate of amide protons in proteins reflects tertiary interactions, not only secondary structure, *Protein Sci. 5*, 653−662.
49. Cavagnero, S., Theriault, Y., Narula, S. S., Dyson, H. J., and Wright, P. E. (2000) Amide proton hydrogen exchange rates for sperm whale myoglobin obtained from 15N-1H NMR spectra, *Protein Sci. 9*, 186−193.
50. Wang, Q. W., Kline, A. D., and Wuthrich, K. (1987) Amide proton exchange in the alpha-amylase polypeptide inhibitor Tendamistat studied by two-dimensional 1H nuclear magnetic resonance, *Biochemistry 26*, 6488−6493.
51. Kalodimos, C. G., Boelens, R., and Kaptein, R. (2002) A residue-specific view of the association and dissociation pathway in protein−DNA recognition, *Nat. Struct. Biol. 9*, 193−197.
52. Wang, C., Pawley, N. H., and Nicholson, L. K. (2001) The role of backbone motions in ligand binding to the c-Src SH3 domain, *J. Mol. Biol. 313*, 873−887.
53. Sivaraman, T., Arrington, C. B., and Robertson, A. D. (2001) Kinetics of unfolding and folding from amide hydrogen exchange in native ubiquitin, *Nat. Struct. Biol. 8*, 331−333.
54. Myszka, D. G., Sweet, R. W., Hensley, P., Brigham-Burke, M., Kwong, P. D., Hendrickson, W. A., Wyatt, R., Sodroski, J., and

Doyle, M. L. (2000) Energetics of the HIV gp120-CD4 binding reaction, *Proc. Natl. Acad. Sci. U.S.A. 97*, 9026−9031.
55. Murphy, K. P., and Freire, E. (1992) Thermodynamics of structural stability and cooperative folding behavior in proteins, *Adv. Protein Chem. 43*, 313−361.
56. Spolar, R. S., and Record, M. T., Jr. (1994) Coupling of local folding to site-specific binding of proteins to DNA, *Science 263*, 777−784.
57. Xie, D., and Freire, E. (1994) Molecular basis of cooperativity in protein folding. V. Thermodynamic and structural conditions for the stabilization of compact denatured states, *Proteins 19*, 291−301.
58. Finnerty, C. M., Chambers, D., Ingraffea, J., Faber, H. R., Karplus, P. A., and Bretscher, A. (2004) The EBP50-moesin interaction involves a binding site regulated by direct masking on the FERM domain, *J. Cell Sci. 117*, 1547−1552.
59. Terawaki, S., Maesaki, R., and Hakoshima, T. (2006) Structural basis for NHERF recognition by ERM proteins, *Structure 14*, 777−789.
60. Burley, S. K., and Petsko, G. A. (1985) Aromatic-aromatic interaction: a mechanism of protein structure stabilization, *Science 229*, 23−28.
61. Kannan, N., and Vishveshwara, S. (2000) Aromatic clusters: a determinant of thermal stability of thermophilic proteins, *Protein Eng. 13*, 753−761.
62. Waters, M. L. (2002) Aromatic interactions in model systems, *Curr. Opin. Chem. Biol. 6*, 736−741.
63. Hofstadter, K., Stuart, F., Jiang, L., Vrijbloed, J. W., and Robinson, J. A. (1999) On the importance of being aromatic at an antibody-protein antigen interface: mutagenesis of the extracellular interferon gamma receptor and recognition by the neutralizing antibody A6, *J. Mol. Biol. 285*, 805−815.
64. Waters, M. L. (2004) Aromatic Interactions in Peptides: Impact on Structure and Function, *Peptide Sci. 76*, 435−445.
65. Gazit, E. (2002) A possible role for pi-stacking in the self-assembly of amyloid fibrils, *FASEB J. 16*, 77−83.
66. Makin, O. S., Atkins, E., Sikorski, P., Johansson, J., and Serpell, L. C. (2005) Molecular basis for amyloid fibril formation and stability, *Proc. Natl. Acad. Sci. U.S.A. 102*, 315−320.
67. Dhe-Paganon, S., Werner, E. D., Nishi, M., Hansen, L., Chi, Y. I., and Shoelson, S. E. (2004) A phenylalanine zipper mediates APS dimerization, *Nat. Struct. Mol. Biol. 11*, 968−974.
68. Hamada, K., Shimizu, T., Yonemura, S., Tsukita, S., Tsukita, S., and Hakoshima, T. (2003) Structural basis of adhesion-molecule recognition by ERM proteins revealed by the crystal structure of the radixin-ICAM-2 complex, *EMBO J. 22*, 502−514.
69. Iwase, A., Shen, R., Navarro, D., and Nanus, D. M. (2004) Direct binding of neutral endopeptidase 24.11 to ezrin/radixin/moesin (ERM) proteins competes with the interaction of CD44 with ERM proteins, *J. Biol. Chem. 279*, 11898−11905.
70. Terawaki, S., Kitano, K., and Hakoshima, T. (2007) Structural basis for type II membrane protein binding by ERM proteins revealed by the radixin-neutral endopeptidase 24.11 (NEP) complex, *J. Biol. Chem. 282*, 19854−19862.
71. Gautreau, A., Poullet, P., Louvard, D., and Arpin, M. (1999) Ezrin, a plasma membrane-microfilament linker, signals cell survival through the phosphatidylinositol 3-kinase/Akt pathway, *Proc. Natl. Acad. Sci. U.S.A. 96*, 7300−7305.
72. Hunter, C. A., Lawson, K. R., Perkins, J., and Urch, C. J. (2001) Aromatic Interactions, *J. Chem. Soc., Perkin Trans. 2*, 651−669.
73. Hunter, C. A., Singh, J., and Thornton, J. M. (1991) Pi-pi interactions: the geometry and energetics of phenylalanine-phenylalanine interactions in proteins, *J. Mol. Biol. 218*, 837−846.
74. Hamada, K., Shimizu, T., Matsui, T., Tsukita, S., and Hakoshima, T. (2000) Structural basis of the membrane-targeting and unmasking mechanisms of the radixin FERM domain, *EMBO J. 19*, 4449−4462.
75. Chen, J., Zhang, Z., Stebbins, J. L., Zhang, X., Hoffman, R., Moore, A., and Pellecchia, M. (2007) A fragment-based approach for the discovery of isoform-specific p38alpha inhibitors, *ACS Chem. Biol. 2*, 329−336.
76. Erlanson, D. A., Wells, J. A., and Braisted, A. C. (2004) Tethering: fragment-based drug discovery, *Annu Rev. Biophys. Biomol. Struct. 33*, 199−223.
77. Rees, D. C., Congreve, M., Murray, C. W., and Carr, R. (2004) Fragment-based lead discovery. *Nat. Rev. Drug Discovery 3*, 660−672.
78. Shuker, S. B., Hajduk, P. J., Meadows, R. P., and Fesik, S. W. (1996) Discovering high-affinity ligands for proteins: SAR by NMR, *Science 274*, 1531−1534.
79. Kitano, K., Yusa, F., and Hakoshima, T. (2006) Structure of dimerized radixin FERM domain suggests a novel masking motif in C-terminal residues 295−304, *Acta. Crystallogr., Sect. F 62*, 340−345.
80. Turunen, O., Wahlstrom, T., and Vaheri, A. (1994) Ezrin has a COOH-terminal actin-binding site that is conserved in the ezrin protein family, *J. Cell Biol. 126*, 1445−1453.
81. Fievet, B. T., Gautreau, A., Roy, C., Del Maestro, L., Mangeat, P., Louvard, D., and Arpin, M. (2004) Phosphoinositide binding and phosphorylation act sequentially in the activation mechanism of ezrin, *J. Cell Biol. 164*, 653−659.
82. Dyson, H. J., and Wright, P. E. (2005) Intrinsically unstructured proteins and their functions, *Nat. Rev. Mol. Cell Biol. 6*, 197−208.
83. Bell, S., Klein, C., Muller, L., Hansen, S., and Buchner, J. (2002) p53 contains large unstructured regions in its native state, *J. Mol. Biol. 322*, 917−927.
84. Dawson, R., Muller, L., Dehner, A., Klein, C., Kessler, H., and Buchner, J. (2003) The N-terminal domain of p53 is natively unfolded, *J. Mol. Biol. 332*, 1131−1141.
85. Kussie, P. H., Gorina, S., Marechal, V., Elenbaas, B., Moreau, J., Levine, A. J., and Pavletich, N. P. (1996) Structure of the MDM2 oncoprotein bound to the p53 tumor suppressor transactivation domain. *Science 274*, 948−953.
86. Rustandi, R. R., Baldisseri, D. M., and Weber, D. J. (2000) Structure of the negative regulatory domain of p53 bound to S100B(betabeta), *Nat. Struct. Biol. 7*, 570−574.
87. Demarest, S. J., Martinez-Yamout, M., Chung, J., Chen, H., Xu, W., Dyson, H. J., Evans, R. M., and Wright, P. E. (2002) Mutual synergistic folding in recruitment of CBP/p300 by p160 nuclear receptor coactivators, *Nature 415*, 549−553.
88. Reeves, R. (2001) Molecular biology of HMGA proteins: hubs of nuclear function. *Gene 277*, 63−81.
89. Reeves, R., and Beckerbauer, L. (2001) HMGI/Y proteins: flexible regulators of transcription and chromatin structure, *Biochim. Biophys. Acta 1519*, 13−29.
90. Zhou, P., Lugovskoy, A. A., McCarty, J. S., Li, P., and Wagner, G. (2001) Solution structure of DFF40 and DFF45 -terminal domain complex and mutual chaperone activity of DFF40 and DFF45, *Proc. Natl. Acad. Sci. U.S.A. 98*, 6051−6055.
91. Huber, A. H., and Weis, W. I. (2001) The structure of the beta-catenin/E-cadherin complex and the molecular basis of diverse ligand recognition by beta-catenin, *Cell 105*, 391−402.
92. Eliezer, D., and Palmer, A. G. 3rd (2007) Biophysics: proteins hunt and gather. *Nature 447*, 920−921.
93. Sugase, K., Dyson, H. J., and Wright, P. E. (2007) Mechanism of coupled folding and binding of an intrinsically disordered protein, *Nature 447*, 1021−1025.
94. Keramisanou, D., Biris, N., Gelis, I., Sianidis, G., Karamanou, S., Economou, A. and Kalodimos, C. G. (2006) Disorder-order folding transitions underlie catalysis in the helicase motor of SecA, *Nat. Struct. Mol. Biol. 13*, 594−602.

BI701281E